Physics of Plasmas

Collisional ionization and recombination effects on coalescence instability in chromospheric partially ionized plasmas

Cite as: Phys. Plasmas **29**, 062302 (2022); https://doi.org/10.1063/5.0087667
Submitted: 08 February 2022 • Accepted: 18 May 2022 • Published Online: 02 June 2022
Published open access through an agreement with JISC Collections

Giulia Murtas, Andrew Hillier and Ben Snow

Physics of Plasmas ARTICLE scitation.org/journal/php

Collisional ionization and recombination effects on coalescence instability in chromospheric partially ionized plasmas

Cite as: Phys. Plasmas **29**, 062302 (2022); doi: 10.1063/5.0087667
Submitted: 8 February 2022 · Accepted: 18 May 2022 ·
Published Online: 2 June 2022

Giulia Murtas,[a] Andrew Hillier, and Ben Snow

AFFILIATIONS

College of Engineering, Mathematics and Physical Sciences, Harrison Building, Streatham Campus, University of Exeter, North Park Road, Exeter EX4 4QF, United Kingdom

[a]Author to whom correspondence should be addressed: gm442@exeter.ac.uk

ABSTRACT

Plasmoid-mediated fast magnetic reconnection plays a fundamental role in driving explosive dynamics and heating, but relatively little is known about how it develops in partially ionized plasmas (PIP) of the solar chromosphere. Partial ionization might largely alter the dynamics of the coalescence instability, which promotes fast reconnection and forms a turbulent reconnecting current sheet through plasmoid interaction, but it is still unclear to what extent PIP effects influence this process. We investigate the role of collisional ionization and recombination in the development of plasmoid coalescence in PIP through 2.5D simulations of a two-fluid model. The aim is to understand whether these two-fluid coupling processes play a role in accelerating reconnection. We find that, in general, the ionization–recombination process slows down the coalescence. Unlike the previous models in Murtas *et al.* [Phys. Plasmas **28**, 032901 (2021)] that included thermal collisions only, ionization and recombination stabilize current sheets and suppress non-linear dynamics, with turbulent reconnection occurring in limited cases: bursts of ionization lead to the formation of thicker current sheets, even when radiative losses are included to cool the system. Therefore, the coalescence timescale is very sensitive to ionization–recombination processes. However, reconnection in PIP is still faster than in a fully ionized plasma environment having the same bulk density: the PIP reconnection rate ($M_{\mathrm{IRIP}} = 0.057$) increases by a factor of $\sim$1.2 with respect to the MHD reconnection rate ($M_{\mathrm{MHD}} = 0.047$).

I. INTRODUCTION

Magnetic reconnection takes place in a wide range of astrophysical settings:[1] it occurs in the presence of a non negligible resistivity, when magnetic field lines change their connectivity altering the topology of the magnetic field. During reconnection, the frozen-in constraint imposed by ideal magnetohydrodynamics (MHD) no longer applies, and the energy released by reconnection energizes particles to high energies and heats the plasma.[2,3] Explosive events in the solar chromosphere, such as chromospheric jets[4,5] and Ellerman bombs,[6,7] are believed to be driven by fast magnetic reconnection, responsible of efficiently releasing the stored magnetic energy into thermal and kinetic energy[2,3] at shorter time scales than the classical reconnection models.

The hypothesis of fast magnetic reconnection as a driver of explosive phenomena in chromospheric plasmas has been reinforced by the identification of plasma blobs in the outflow of chromospheric jets and UV bursts,[8–10] colliding and merging with each other before being ejected from the current sheet. These structures are generally interpreted to be plasmoids, concentrations of current density trapped in closed loops of magnetic field lines that are commonly present in reconnecting systems.[11–17] Plasmoids are believed to play a major role in speeding up reconnection to the time scales found in observations, as their formation directly affects the current sheet size.[18] Plasmoids can be the result of the tearing instability, which breaks thin current sheets (where the current sheet aspect ratio is $\delta/L \ll 1$) into fragments.[11,15,19] The resulting high current densities in each of these fragments facilitate a high reconnection rate.[20]

Plasmoid formation due to the instability of current sheets has been extensively examined through numerical studies.[17,21–27] This mechanism is dependent on the value of the Lundquist number,[13,28,29] $S = \frac{Lv_A}{\eta}$, where L is a characteristic length of the system, v_A is the Alfvén speed, and η is the diffusivity. Several works proved that it is

possible to speed up reconnection in thin current sheets for a critical value of the Lundquist number typically $\sim 10^3$–10^4 for fully ionized plasmas.[14,16,17,20,27,30–35] Above this limit, current sheets become unstable, and plasmoids formation occurs.

Once plasmoids are generated, they are pulled against each other and merge, in a mechanism that further increases the reconnection rate: this process is called coalescence instability.[2,36] Plasmoid coalescence occurs in the nonlinear tearing mode phase between plasmoids sharing an X-point and evolves through two separate phases. The first is an ideal MHD phase with a growth rate that is almost independent of η.[36] In this phase, the two plasmoids move close, and a current sheet forms between them. The second part of coalescence evolves in a resistive phase, where the current sheet begins to reconnect.[2] As further plasmoids are formed in between the coalescing plasmoids, this instability can become a fractal process operating at multi-spatial scale, depending on the Lundquist number.[13,28,29]

A large portion of plasmas across the universe are only partially ionized, for example, the chromospheric plasma, whose ionization degree falls in the range 10^{-4}–10^{-1}, as reported by many studies.[20,37–40] The presence of neutral species might alter the plasmoid dynamics, as further physical processes develop from the coupling with charged particles. The role of partial ionization on the onset of magnetic reconnection and resistive tearing instability was investigated in several studies.[8,18,20,41–44] It has been observed that partial ionization largely modifies the reconnection rate by changing the Alfvén speed, which, in turn, affects the Lundquist number of the system[42] and the conditions for plasmoids formation.

The physics of a reconnecting current sheet is also affected by processes of collisional ionisation[45] and recombination, which actively modify the relative abundance of the plasma species. As pointed out from many studies of magnetic reconnection in a multi-fluid partially ionized plasma at low β,[7,42,43,46–48] the non-equilibrium ionization–recombination leads to a strong ionization of the material in the reconnection region, and a faster reconnection rate develops before the onset of plasmoid instabilities.[48] Past studies[43] reported an increase in the ionization degree by an order of magnitude within the current sheet during reconnection. The strong ionization is responsible for a larger interaction between the neutral fluid and the plasma, with a stronger coupling occurring both in the inflow and outflow regions. In the case of a plasma β smaller than 1, however, plasmoid instability remains the main process promoting fast magnetic reconnection.[48]

The ionization–recombination effects are further enhanced by the action of the ionization potential. When collisional ionization takes place, the energy expended by a free electron to release a bound electron results in a net loss of energy from the plasma.[49] As the recombination process is associated with changes in energy levels and photons being released, this overall effect can be modeled as a radiative loss. Studies investigating the role of radiative cooling in magnetic reconnection[50,51] proved that the inclusion of the ionization potential thins the reconnection layer by decreasing the plasma pressure and density inside the current sheet. Therefore, adding radiative losses speeds up reconnection to higher rates than the ones of models without radiation and might lead to time scales and outflows that are consistent with those found in spicules and chromospheric jets.[52]

Relatively little is known about how the coalescence instability is altered by the multi-fluid physics of a partially ionized plasma. In our preliminary study,[53] we found that, in an ion-neutral plasma with fluids coupled through elastic collisions, partial ionization speeds up both phases of coalescence and promotes non-linear effects during reconnection. In this paper, we examine in detail the effects of collisional ionization, recombination, and optically thin radiative losses on the coalescence instability developing in partially ionized plasmas. This model improves upon our previous work[53] by including the contribution of these processes. We aim to understand how the new type of coupling between charges and neutral species influences the reconnection rate, compared to our previous research. In Sec. II, we discuss the two-fluid model employed for our simulations. In Sec. III, we report the results of our 2.5D simulations. The results are discussed in Sec. IV.

II. METHODS

Numerical simulations are performed of the coalescence instability in 2.5D using the (PIP) code.[54] The process is studied in single-fluid fully ionized cases (MHD) and two-fluid partially ionized cases (PIP). MHD cases are modeled by a charge-neutral ion-electron hydrogen plasma, while PIP cases are characterized by a neutral fluid and a hydrogen plasma being collisionally coupled. The fluids are described by two separate sets of non-dimensional equations,[55] which have been derived from previous models.[42,56,57] The equations are solved throughout the domain through a fourth-order central difference scheme, and the physical variable updates are computed by a four-step Runge–Kutta[58] scheme for time integration. The neutral fluid is governed by compressible inviscid hydrodynamics equations:

$$\frac{\partial \rho_n}{\partial t} + \nabla \cdot (\rho_n \mathbf{v}_n) = D, \tag{1}$$

$$\frac{\partial}{\partial t}(\rho_n \mathbf{v}_n) + \nabla \cdot (\rho_n \mathbf{v}_n \mathbf{v}_n + p_n \mathbf{I}) = \mathbf{R}, \tag{2}$$

$$\frac{\partial e_n}{\partial t} + \nabla \cdot [\mathbf{v}_n (e_n + p_n)] = E, \tag{3}$$

$$e_n = \frac{p_n}{\gamma - 1} + \frac{1}{2}\rho_n v_n^2, \tag{4}$$

$$T_n = \gamma \frac{p_n}{\rho_n}, \tag{5}$$

while compressible inviscid resistive MHD equations model the plasma

$$\frac{\partial \rho_p}{\partial t} + \nabla \cdot (\rho_p \mathbf{v}_p) = -D, \tag{6}$$

$$\frac{\partial}{\partial t}(\rho_p \mathbf{v}_p) + \nabla \cdot \left(\rho_p \mathbf{v}_p \mathbf{v}_p + p_p \mathbf{I} - \mathbf{B}\mathbf{B} + \frac{\mathbf{B}^2}{2}\mathbf{I}\right) = -\mathbf{R}, \tag{7}$$

$$\frac{\partial}{\partial t}\left(e_p + \frac{B^2}{2}\right) + \nabla \cdot \left[\mathbf{v}_p (e_p + p_p) - (\mathbf{v}_p \times \mathbf{B}) \times \mathbf{B} + \eta (\nabla \times \mathbf{B}) \times \mathbf{B}\right] = -E - \Phi_I + A_{heat}, \tag{8}$$

$$\frac{\partial \mathbf{B}}{\partial t} - \nabla \times (\mathbf{v}_p \times \mathbf{B} - \eta \nabla \times \mathbf{B}) = 0, \tag{9}$$

$$e_p = \frac{p_p}{\gamma - 1} + \frac{1}{2}\rho_p v_p^2, \tag{10}$$

$$\nabla \cdot \mathbf{B} = 0, \tag{11}$$

$$T_p = \gamma \frac{p_p}{2\rho_p}. \tag{12}$$

The subscripts p and n in both plasma and neutral equations identify physical quantities of the ion-electron plasma and the neutral fluid, respectively. The variables $\mathbf{v}$, p, ρ, T, and e are, respectively, the fluids velocity, gas pressure, density, temperature, and internal energy, $\gamma = 5/3$ is the adiabatic index, and $\mathbf{B}$ is the magnetic field. The terms D, $\mathbf{R}$, and E are, respectively, the source terms for mass, momentum, and energy transfer between the two species and are defined as follows:

$$D = \Gamma_{rec}\rho_p - \Gamma_{ion}\rho_n, \tag{13}$$

$$\mathbf{R} = -\alpha_c\rho_n\rho_p(\mathbf{v}_n - \mathbf{v}_p) + \Gamma_{rec}\rho_p\mathbf{v}_p - \Gamma_{ion}\rho_n\mathbf{v}_n, \tag{14}$$

$$E = -\alpha_c\rho_n\rho_p\left[\frac{1}{2}(\mathbf{v}_n^2 - \mathbf{v}_p^2) + \frac{T_n - T_p}{\gamma(\gamma-1)}\right] + \frac{1}{2}(\Gamma_{rec}\rho_p\mathbf{v}_p^2 - \Gamma_{ion}\rho_n\mathbf{v}_n^2) + \frac{\Gamma_{rec}\rho_p T_p - \Gamma_{ion}\rho_n T_n}{\gamma(\gamma-1)}. \tag{15}$$

Both fluids are subject to the ideal gas law. The factor of 2 in Eq. (12) is included to account for the electron pressure in the plasma contribution.

The two-fluid collisional coupling is determined by the parameter $\alpha_c(T_n, T_p, \nu_D)$, whose non-dimensional expression,[59] which includes charge exchange,[60] is found in the following equation:

$$\alpha_c = \alpha_c(0)\sqrt{\frac{T_n + T_p}{2}}\sqrt{1 + \frac{9\pi}{64}\frac{\gamma}{2(T_n + T_p)}\nu_D^2}, \tag{16}$$

where $\alpha_c(0)$ is the initial coupling and $\nu_D = |\mathbf{v_n} - \mathbf{v_p}|$ is the magnitude of the drift velocity between the neutral components and the hydrogen plasma. When the magnitude of the drift velocity becomes bigger than the thermal velocity, the particles are subject to a higher number of collisions as they are drifting past each other: the expression for α_c in Eq. (16) takes into account the higher number of collisions occurring at supersonic drift velocities. The collisional coupling between ions and electrons is modeled by imposing a spatially uniform, constant diffusivity (η) in the system. The two fluids are in an initial thermal equilibrium, but there is not an imposed initial ionization equilibrium. The Hall effect is not included in this study.

The terms Γ_{rec} and Γ_{ion} are the recombination and collisional ionization rates for a hydrogen atom. The normalized empirical forms of the rates[45,61] are

$$\Gamma_{rec} = \frac{\rho_p}{\sqrt{T_p}}\frac{\sqrt{T_f}}{\xi_p(0)}\tau_{\mathrm{IR}}, \tag{17}$$

$$\Gamma_{ion} = \rho_p\left(\frac{e^{-\chi}\chi^{0.39}}{0.232 + \chi}\right)\frac{\hat{R}}{\xi_p(0)}\tau_{\mathrm{IR}}, \tag{18}$$

where

$$\chi = 13.6\frac{T_f}{T_{e0}T_p}, \tag{19}$$

$$\hat{R} = \frac{2.91\cdot 10^{-14}}{2.6\cdot 10^{-19}}\sqrt{T_{e0}}. \tag{20}$$

The rates of collisional ionization used in this work are based on a semi-empirical model for the ionization of hydrogen by electron impact that assumes ionization from the ground state.[45,62,63] These rates do not include photo-ionization or ionization from excited states, which are known to be important for the chromosphere.[64–66]

Two characteristic temperatures appear in Eqs. (17)–(20) and are based on a physical reference electron temperature T_0 in K. T_{e0} is the value of T_0 converted in electron volts. The initial normalization of the system gives a bulk sound speed of unity. However, in the two-fluid model, this does not necessarily equate to a plasma temperature of unity. The ionization and recombination rates depend on the electron temperature (which is assumed to be equal to the plasma temperature in our model); therefore, a correction factor T_f is needed to ensure that the desired dimensional electron temperature is being used to calculate the rates. For our normalization, the plasma temperature is defined as

$$T_p = \frac{\gamma p_p}{2\rho_p} = \frac{\gamma}{2}\frac{2\xi_p}{(\xi_n + 2\xi_p)}\frac{p_p + p_n}{\xi_p(\rho_p + \rho_n)}, = \frac{\gamma(p_p + p_n)}{\rho_p + \rho_n}\frac{1}{\xi_n + 2\xi_p} = \frac{\gamma(p_p + p_n)}{\rho_p + \rho_n}\frac{1}{T_f}, \tag{21}$$

where $\gamma(p_p + p_n)/(\rho_p + \rho_n)$ is the bulk sound speed squared and is initially equal to 1. Therefore, the factor T_f is applied to ensure that the electron (plasma) temperature used in the ionization–recombination rates corresponds initially to the reference dimensional temperature T_0.

The initial ion fraction ξ_p is determined from the initial choice of the temperature T_0 through its relation with ionization and recombination rates. In a steady state, the source term for mass D in Eq. (13) is zero, leading to the following relation:

$$\Gamma_{rec}\rho_p = \Gamma_{ion}\rho_n. \tag{22}$$

Rearranging the terms in Eq. (22), we obtain

$$\xi_p = \frac{1}{1 + \frac{\Gamma_{rec}}{\Gamma_{ion}}}. \tag{23}$$

Ionization and recombination rates can be expressed as a function of the temperature T and the plasma density ρ_p

$$\Gamma_{ion} = G(T)\rho_p, \tag{24}$$

$$\Gamma_{rec} = F(T)\rho_p, \tag{25}$$

therefore, the ion fraction can be also expressed as a function of the temperature

$$\xi_p = \frac{1}{1 + \frac{F(T)}{G(T)}}. \tag{26}$$

In the case of simulations not including ionization–recombination processes, ξ_p is imposed as an initial condition.

The free parameter τ_{IR} determines the relation of the recombination timescale with the dynamic timescale of the simulation, calculated from a characteristic length and a characteristic speed of the system (see later in the section for more details). In the (PIP) code, Γ_{ion} and Γ_{rec} are calculated in the dimensional form from Eqs. (17) and (18) and then normalized by the recombination rate in order to obtain an initial $\Gamma_{rec} = 1$. The parameter τ_{IR} is imposed to re-scale Γ_{rec} and fix an initial recombination timescale. For example, if τ_{IR} is set equal to 10^{-3}, then the initial $\Gamma_{rec} = 10^{-3}$, and recombination would occur over a timescale of 10^3. The ionization rate Γ_{ion} is also normalized by the same τ_{IR}.

The terms Φ_I and A_{heat} in Eq. (8) are associated with the ionization potential and account for radiative losses. Φ_I approximates the energy removed by the system through ionization, while A_{heat} is an arbitrary heating term included to obtain an initial equilibrium. Their non-dimensional forms are

$$\Phi_I = \Gamma_{ion}\rho_n\hat{\Phi}, \tag{27}$$

$$A_{heat} = \Gamma_{ion}(t=0)\rho_n(t=0)\hat{\Phi}, \tag{28}$$

where $\hat{\Phi} = 13.6/(K_B\gamma T_0)$ ensures consistency between the normalization of ionization potential and the equations modeling the system. Here, the Boltzmann constant is $K_B = 8.617 \times 10^{-5}\,\mathrm{eV\,K^{-1}}$. More details on the atomic internal structure used to estimate the ionization potential can be found in a recent paper.[49]

Both sets of equations are non-dimensionalised[55] by a reference density ρ_0 and the total sound speed $c_s = \sqrt{\gamma(p_n + p_p)/(\rho_n + \rho_p)}$, initially set equal to 1. For fully ionized plasmas (MHD cases), the initial density and pressure are set constant, uniform across the domain and equal to

$$\rho_{\mathrm{MHD}} = \xi_p\rho_0 = 1, \tag{29}$$

$$p_{\mathrm{MHD}} = p_0 = \gamma^{-1}, \tag{30}$$

where ξ_p is the ion fraction, equal to 1 for fully ionized plasmas. The cases that are run in a partially ionized plasma (PIP cases) present a similar normalization as the one for a fully ionized plasma, where the bulk physical variables are set equal to the MHD values and uniform across the domain,

$$\rho_n + \rho_p = \xi_n\rho_0 + \xi_p\rho_0 = 1, \tag{31}$$

$$p_n + p_p = \frac{\xi_n}{(\xi_n + 2\xi_p)}p_0 + \frac{2\xi_p}{(\xi_n + 2\xi_p)}p_0 = \gamma^{-1}, \tag{32}$$

where ξ_n is the neutral fraction.

This normalization is chosen to have the physical properties dependent on characteristic length scales, which are directly comparable to the size of the plasmoids involved in the merging. The non-dimensional collision frequency can be compared to the chromospheric dimensional values by dividing it by a characteristic dimensional timescale τ_{col}. The parameter τ_{col} is found from the ratio of the physical plasmoid size (see Sec. II A for more details) and a characteristic speed in the solar chromosphere, which, in this study, is chosen to be the sound speed ($\sim$10 km s^{-1}). Therefore, the model can be easily re-scaled to examine the properties of magnetic structures of various sizes in the solar chromosphere, from a few meters to a few hundred kilometers.

A. Initial conditions

The initial setup of plasmoid coalescence is provided by a modified force-free Fadeev equilibrium,[2,67] with the magnetic field components given by Eqs. (33)–(35). Despite the photospheric magnetic field not being force-free at the boundary with the convective zone, its structure is rearranged before reaching the corona as the non force-free components decay due to the action of chromospheric neutrals.[68] For this reason, it is useful to impose an initial force-free field condition to the system. The classic Fadeev equilibrium magnetic field does not satisfy the condition $\mathbf{J}\times\mathbf{B} = 0$ for a force-free field. Therefore, the traditional Fadeev equilibrium is modified by including a component B_z,

$$B_x = -\frac{\sqrt{2\gamma^{-1}\beta^{-1}}\varepsilon\sin(kx)}{\cosh(ky) + \varepsilon\cos(kx)}, \tag{33}$$

$$B_y = -\frac{\sqrt{2\gamma^{-1}\beta^{-1}}\sinh(ky)}{\cosh(ky) + \varepsilon\cos(kx)}, \tag{34}$$

$$B_z = \frac{\sqrt{2\gamma^{-1}\beta^{-1}}\sqrt{1-\varepsilon^2}}{\cosh(ky) + \varepsilon\cos(kx)}. \tag{35}$$

In the equations above, $k = \frac{\pi}{2}$ and $\varepsilon = 0.5$ lead to a moderately peaked current localization at each plasmoid center. In the limit for $\varepsilon \to 0$, there is a less peaked current density and a weaker attraction between the plasmoids. When $\varepsilon = 0$, B_y reduces to a current sheet characterized by the tanh profile of the well known Harris sheet.[69] The limit $\varepsilon \to 1$ corresponds to a peaked localization and stronger attraction forces. At the upper limit ($\varepsilon = 1$), the current distribution becomes the delta function. The bulk (plasma + neutrals) plasma β, defined as $2(p_p + p_n)/B^2$, is set equal to 0.1 for all simulations. In the two-fluid cases, it is possible to define a second plasma β associated with the isolated plasma $2p_p/B^2$, which, from the initial condition, is equal to 0.002. The initial current density distribution and magnetic field lines are shown in Fig. 1. Note that these initial conditions mimic our previous paper.[53]

The Fadeev equilibrium is unstable to the coalescence instability.[2] An initial velocity perturbation in both plasma and neutral species is imposed to break the initial equilibrium, given by

$$v_{x,p} = v_{x,n} = -0.05\sin\left(\frac{kx}{2}\right)e^{-y^2} + v_{\mathrm{noise}}, \tag{36}$$

where v_{noise} is a white noise component two orders of magnitude smaller than the main perturbation, included to simulate small environmental perturbations. The smaller magnitude of the white noise prevents it from dominating the motion of the two plasmoids during coalescence, while still promoting smaller scale dynamics by breaking the symmetry of the system. All simulations were performed with the same random noise seed. The sin(x) term promotes attraction of the plasmoids, while the term dependent on y localizes the perturbation to a small region around the x-axis. Further details on the chosen velocity perturbation can be found in our recent paper.[53]

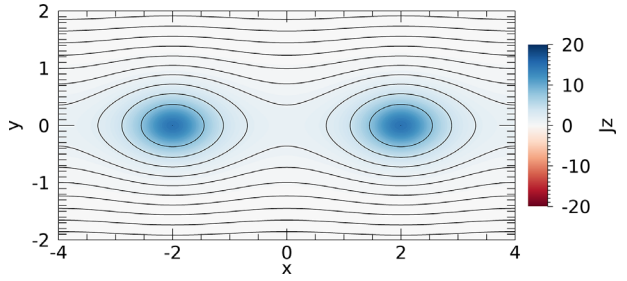

FIG. 1. Initial distribution for the current density J_z ($t = 0$). The center of the two initial plasmoids (blue spots) is located on the x-axis. Magnetic field lines are displayed in black.

All simulations are resolved by 4100×3074 grid cells, corresponding to a cell size of $\Delta x = 1.95 \times 10^{-3}$ and $\Delta y = 2.6 \times 10^{-3}$. The resolution has been tested in order to ensure that the current sheets are resolved with our grid. The initial separation between the plasmoids, calculated from O-point to O-point (the center of the blue spots in Fig. 1) is equal to $4L$, where L is resolved by 513 grid points. The initial plasmoids width, calculated as the distance between top and bottom edges of the separatrix, is $1.66L$ and determined by the initial magnetic field conditions.

The dynamics of the plasmoids merging is evaluated in a squared computational domain of $x = [-4, 4]$ and $y = [-4, 4]$. We use symmetric boundaries at $y = -4$ and $y = 4$: in this configuration, v_x and B_y change sign across the boundary, while v_y and B_x keep the same magnitude and sign across the boundary. The boundaries at $x = -4$ and $x = 4$ are chosen to be periodic.

III. RESULTS

The coalescence instability has been well studied in MHD.[2,36,70–73] The general behavior is that neighboring plasmoids inside a current sheet attract each other, a second current sheet forms in between them, and reconnection occurs in it, leading to the plasmoids complete merging. Extending the model to PIP (using only thermal collisions) results in a faster coalescence and the promotion of small-scale dynamics such as sub-critical secondary plasmoids formation and fractal coalescence (see our recent paper[53]). Here, the model is further extended to account for ionization/recombination and ionization potential effects, which provide a more realistic description of the physical processes occurring in a partially ionized plasma.

Initially, results are presented for weakly coupled PIP cases with elastic collisions only (NIR), ionization and recombination (IR), and ionization, recombination, and ionization potential (IRIP), which are compared to a fiducial MHD simulation. Figure 2 shows the time evolution of the coalescence through the current density for reference cases A1 (NIR), A2 (IR), and A3 (IRIP), corresponding to the three models for PIP. From this figure, we see major differences among NIR, IR, and IRIP cases in timescale, the reconnection rate, and dynamics of each phase of coalescence. These results are discussed in detail in Sec. III A. A parameter study is then performed in Sec. III D to investigate the effect of varying τ_{IR}, which determines the relative importance of ionization and recombination rates to the collision rates, and on the initial ion fraction in Sec. III E. The full array of simulations is shown in Table I. Simulations listed with letter M are run in fully ionized plasmas (MHD). Cases listed with letter A are the reference PIP simulations for the comparison of PIP coupling models. Cases listed with letter B compose the survey on τ_{IR}. Cases listed with letter C compose the survey on the initial ion fraction $\xi_p(0)$.

A. Current sheet and reconnection rate

We analyze three PIP cases (listed as A1, A2, and A3 in Table I) where different coupling terms are included in each simulation: A1 corresponds to a PIP case with elastic collisions only (NIR), and its parameters are set equal to the reference PIP cases examined in our previous work;[53] A2 includes ionization and recombination processes (IR); A3 includes the ionization potential (IRIP). In the cases with ionization and recombination processes (A2 and A3), we set $\tau_{IR} = 10^{-3}$. By choosing this value for τ_{IR}, the ratio of the collision time to recombination time is 10^{-5}, which is consistent with chromospheric rates.[49,74] Based on the initial conditions, neutral–ion collisions occur on timescales of $\Delta t = (\alpha_c \rho_p)^{-1} = 1$, ion-neutral collisions on timescales of $\Delta t = (\alpha_c \rho_n)^{-1} \sim 0.01$, and recombination on time scales of $\Delta t = 10^3$.

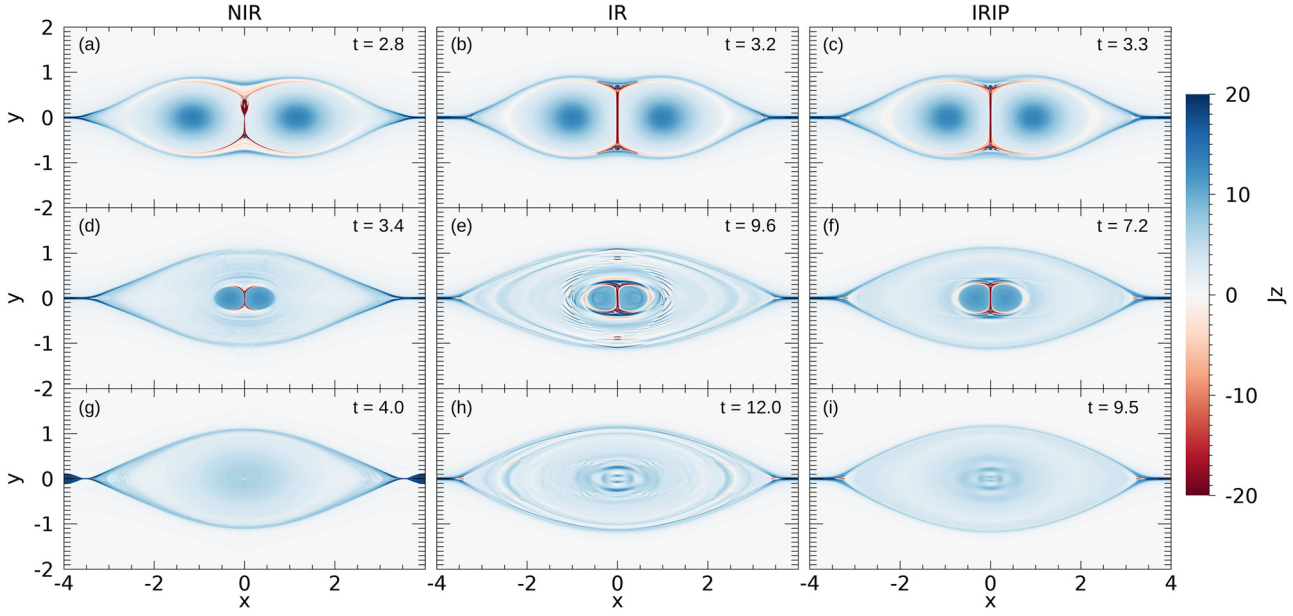

FIG. 2. Comparison of Jz between three PIP cases with different two-fluid coupling processes: NIR (A1, left column), IR (A2, central column), and IRIP (A3, right column). The frames identify different steps of the coalescence instability. Panels (a)–(c) show the initiation of the reconnection process. In panels (d)–(f), the evolution of coalescence is displayed at later stages. The final stage of coalescence is shown in panels (g)–(i) with the formation of the resulting plasmoid. Times are given in the same non-dimensional unit.

TABLE I. List of simulations parameters.

ID	Model	η	α_c (0)	ξ_p [b] (0)	T_0 (K)[b]	τ_{IR}
M1	MHD	1.5×10^{-3}	∞[a]	1[a]	...	...
M2	MHD	3×10^{-3}	∞[a]	1[a]	...	...
A1	NIR	1.5×10^{-3}	10^2	10^{-2}	10 855	...
A2	IR	1.5×10^{-3}	10^2	10^{-2}	10 855	10^{-3}
A3	IRIP	1.5×10^{-3}	10^2	10^{-2}	10 855	10^{-3}
B1	IRIP	1.5×10^{-3}	5	10^{-2}	10 855	5×10^{-6}
B2	IRIP	1.5×10^{-3}	5	10^{-2}	10 855	5×10^{-5}
B3	IRIP	1.5×10^{-3}	5	10^{-2}	10 855	5×10^{-4}
B4	IRIP	1.5×10^{-3}	5	10^{-2}	10 855	5×10^{-3}
B5	IRIP	1.5×10^{-3}	5	10^{-2}	10 855	5×10^{-2}
B6	IRIP	1.5×10^{-3}	5	10^{-2}	10 855	5×10^{-1}
B7	IRIP	5×10^{-4}	5	10^{-2}	10 855	5×10^{-5}
B8	IRIP	5×10^{-4}	5	10^{-2}	10 855	5×10^{-4}
B9	IRIP	5×10^{-4}	5	10^{-2}	10 855	5×10^{-3}
C1	IRIP	1.5×10^{-3}	5	2×10^{-3}	9855	5×10^{-5}
C2	IRIP	1.5×10^{-3}	5	4×10^{-2}	11 855	5×10^{-5}
C3	IRIP	1.5×10^{-3}	5	10^{-1}	12 855	5×10^{-5}

[a]These data are the effective values of the two-fluid parameters α_c and ξ_p for the single-fluid cases, which are chosen as limits for the PIP simulations.
[b]ξ_p (0) and T_0 are not independent variables. The initial ion fraction is determined by setting the value for T_0 at the beginning of the calculation.

The coalescence instability is shown in Fig. 2 at three different stages of development. In the first phase of the process, the plasmoids come together, and when the oppositely directed magnetic field lines are pushed against each other, a current sheet forms in the center of the domain. In the first row of panels (a)–(c) corresponding to the end of this first phase of coalescence, the current sheet appears as the thin red vertical region at $x = 0$. After the current sheet formation, reconnection begins, and the current sheet slowly reduces in length, together with the decrease in size of the plasmoids. The reconnected field lines form an envelope that surrounds the two merging plasmoids and constitutes the external boundary of the final plasmoid resulting from the coalescence. The second row of panels (d)–(f) shows the plasmoid merging at these later stages, while the third row (g)–(i) displays the end of coalescence and the larger merged plasmoid.

Each row of panels in Fig. 2 allows to compare the three PIP cases at similar stages of coalescence. Panels (a)–(c) show the current sheet structure and early small-scale dynamics at the beginning of the reconnection phase. The current sheet thickness δ is estimated by taking the full width at 1/8 of the maximum current density J_z along the x-axis ($y = 0$): this particular ratio is chosen to be consistent with the analysis previously performed on 2.5D calculations.[53] A first difference between the three cases is observed in δ at the stage displayed by panels (a)–(c). The current sheet thickness for case A1 is $\delta_{NIR} = 0.018$ (~9 grid points), while $\delta_{IR} = 0.045$ (~23 grid points) and $\delta_{IRIP} = 0.029$ (~15 grid points) for cases A2 and A3, respectively. Case A1 displays the thinner current sheet, and it is also the only case where the tearing instability develops. The inclusion of ionization and recombination processes stabilizes the current sheet against the tearing instability, as the plasma density increases in the reconnecting current sheet following a burst in ionization [panels (b) and (c) of Fig. 2]. Varying the type of coupling between the fluids, from elastic collisions only to the inclusion of Γ_{ion}, Γ_{rec}, and ionization potential, the coalescence dynamics also drastically changes. Formation and expulsion of large secondary plasmoids are observed in panel (a) of Fig. 2 for case A1. No plasmoids form in cases A2 and A3.

The coalescence timescale varies when varying the type of coupling between the fluids, as shown by panels (g)–(i) where the final stage of the merging is displayed. Figure 3 shows the time variation of the current density at the center of the current sheet for simulations A1, A2, and A3. These are compared to a single uid MHD case (listed as M1 in Table 1). M1 can be treated as the limit for a completely coupled system ($\alpha_c \to \infty$, $\tau_{IR} \to \infty$), where density and pressure are assumed to be equal to the bulk (ion + neutral) values. The beginning of the reconnection phase is identified in all curves in Fig. 3 by the first minimum in the current density. The formation of the central current sheet begins at similar times for all PIP simulations, suggesting that ionization and recombination rates effects become relevant in the coalescence dynamics only once the current sheet is formed. During the initial phase of coalescence, the temperature is roughly constant, and hence, Γ_{ion} and Γ_{rec} do not vary much. During the second phase, where compressional, Ohmic, and frictional heating become substantial, the temperature variation results in greatly enhanced ionization and recombination rates [see Eqs. (17) and (18)].

Figure 4 shows the mean plasma and neutral temperature in the current sheet of our fiducial MHD and PIP simulations as they vary with time. Initially, the temperature spikes in all simulations as the current sheet collapses, due to a combination of compressional and Ohmic heating, which dominate inside the current sheet, and frictional heating. The values for T_p and T_n in case A1 (NIR model) are consistent with the ones found in our previous study.[53] The large increase in both plasma and neutral temperatures results from the small value of the ion plasma β and the rarefaction of the reconnection region, where the density of both fluids is very low. The neutral rarefaction observed in case A1, consistent with the results shown in Fig. 4 of our previous work,[53] is the result of a strong divergence of the neutral velocity field. This divergence reaches values of 1.6 inside the forming current sheet at $t = 2$ and increases to be 16.7 at $t = 2.4$ and occurs because the

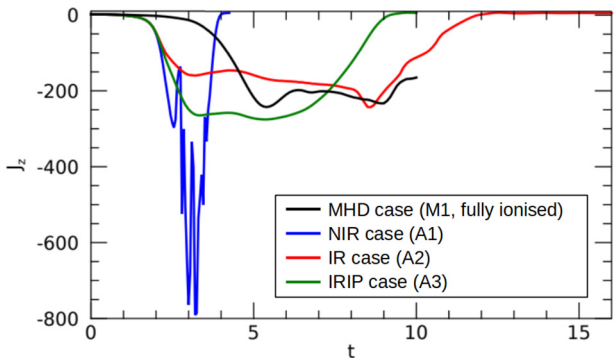

FIG. 3. Time evolution of current density J_z at the center of the current sheet for the PIP cases A1, A2, and A3 with $\alpha_c = 100$. The NIR case (blue), IR case (red), and IRIP (green) are compared to a MHD case (M1, black line), included as reference for the limit case of completely coupled fluids ($\alpha_c \to \infty$). The IR and IRIP cases are run at $\tau_{IR} = 10^{-3}$.

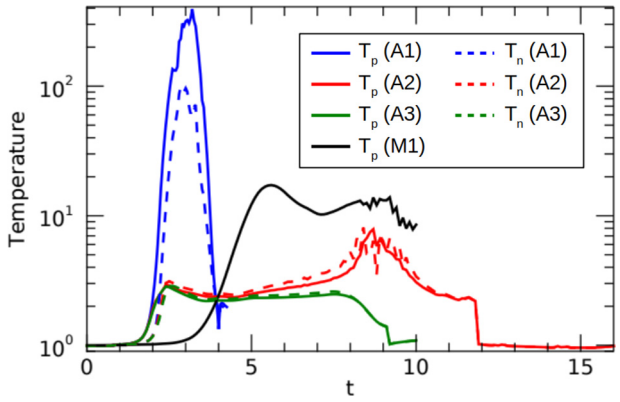

FIG. 4. Time variation of the mean plasma and neutral temperatures inside the current sheet for the PIP cases A1 (blue), A2 (red), and A3 (green), and the mean plasma temperature inside the current sheet of the MHD case M1 (black). Plasma temperatures are identified by the solid lines, and neutral temperatures are identified by the dashed lines.

neutrals are subject to two forces, generated by the drag from the plasma and by the neutral pressure, respectively. As it is shown in our recent paper[53] shows, the neutral pressure gradient works against the drag force to hinder the neutral inflow, but it works with the drag to promote the acceleration of the material in the outflow. As a result, the neutrals are able to leave the current sheet faster than they enter, resulting in the current sheet becoming rarefied.

In cases A2 (IR model) and A3 (IRIP model), both T_p and T_n are much lower than case A1, and there is far less temperature difference between the two species. This happens because the strong heating in the current sheet has a large effect on the ionization–recombination rates, which, in turn, act on the current sheet thickness: the high ionization rate converts neutrals to plasma, which results in the current sheet thinning less, J_z is smaller than NIR cases (as shown in Fig. 3), and the Ohmic heating is smaller, thus leading to a cooler plasma.

In our equilibrium plasma at $t = 0$, the rates of both cases A2 and A3 are $\Gamma_{ion} = 10^{-5}$ and $\Gamma_{rec} = 10^{-3}$, and ionization and recombination happen on time scales of $\Delta t \sim 10^5$ and 10^3, respectively; in our current sheet, ionization happens on time scales of $\Delta t \sim 0.02$ for case A2 ($\Gamma_{ion} = 47.12$) and 0.05 for case A3 ($\Gamma_{ion} = 19.54$), while recombination occurs on time scales of $\Delta t \sim 8$ for both cases ($\Gamma_{rec} = 0.13$ in A2 and 0.12 in A3). This means that, for both cases A2 and A3, Γ_{ion} varies of about 6 orders of magnitude, while Γ_{rec} varies of about 2 orders of magnitude from the initial phase to the reconnection phase. As the ionization rate increases, so do the energy losses due to ionization potential. The ionization potential term acts to remove energy from the plasma, hence lowers T_p. In case A3, the cooling action of the ionization potential contributes to further decrease both T_p and T_n compared to case A2. Including the physics of ionization, recombination and ionization potential leads to a more realistic description of the system, with a temperature variation of a factor of 3 rather than a factor of 400 as observed for the NIR model.

The end of the merging is identified for each case in Fig. 3 by the current density acquiring a positive value again at later times, after the development of large negative currents during the reconnection phase. The fastest coalescence occurs in case A1 (blue curve in Fig. 3). The shorter timescale depends on the onset of turbulent reconnection, as the secondary plasmoids expelled from the current sheet allow a more efficient release of magnetic flux. Turbulent reconnection leads to a larger J_z magnitude: the large fluctuations occurring at $t > 2.8$ are produced by secondary plasmoids forming and being ejected from the current sheet. In both cases A2 (red) and A3 (green), reconnection occurs laminarly, similar to the MHD simulation. The coalescence timescale shortens at the inclusion of the ionization potential. This is shown by both the comparison of the final time in panels (h) and (i) in Fig. 2 and the comparison between green and red curves in Fig. 3. The shortening of the coalescence timescale occurs as the cooling of the ionization potential results in the recombination of a large portion of ions and consequently a thinner current sheet.

Figure 5 shows the reconnection rate for simulations A1 (blue), A2 (red), and A3 (green) compared to the fully ionized plasma case M1 (black), where the reconnection rate is given by

$$M = \frac{\eta J_{\max}}{v_A B_{up}}. \tag{37}$$

In Eq. (37) J_{max} is the maximum absolute value of the current density inside the current sheet, v_A is the initial maximum value of the bulk Alfvén speed, and B_{up} is the initial maximum value of B_y in the inflow. Comparing the trend of the reconnection rate in Fig. 5 with the evolution of the current density previously shown in Fig. 3, it is evident that for case A1, the reconnection rate shows far less fluctuation than J_z. This comes from the definition of the reconnection rate, which depends on J_{max}: the maximum current density inside the current sheet is not necessarily occurring at its center at all times, and this is particularly evident in the case of secondary plasmoids production. While we had fixed the calculation of J_z at the center to evaluate the type of reconnection developing in the current sheet, we now want to examine the maximum reconnection rate that is achieved within the current sheet.

The mean reconnection rate of case A1, where the fluids are coupled through elastic collisions and charge exchange only, is approximately $M_{\rm NIR} = 0.12 \pm 0.05$: in this case, the reconnection rate displays very sharp variations during the merging following the formation and ejection of the secondary plasmoids. The stabilization of the current sheet by the action of ionization and recombination is reflected in the lower peak value and flatter trend of the reconnection rate for

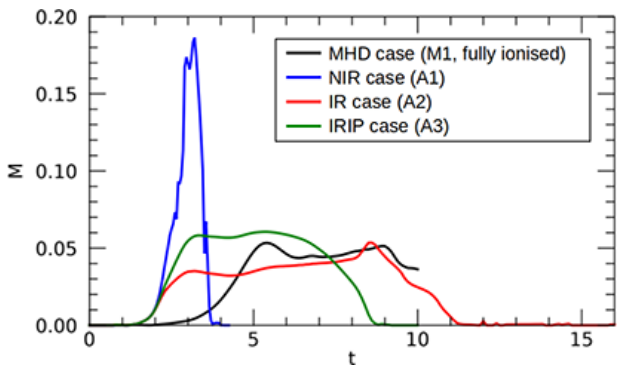

FIG. 5. Time variation of the reconnection rate for the PIP cases A1 (blue), A2 (red), and A3 (green), and the MHD case M1 (black).

the cases A2 and A3, where secondary plasmoids do not form and whose smoother fluctuations can be compared to the MHD case. The mean reconnection rates of cases A2 and A3 are also comparable to the MHD rate, $M_{MHD} = 0.047 \pm 0.003$. In case A2, $M_{IR} = 0.038 \pm 0.006$, lower than the fully ionized case. As already shown by the current density in Figs. 2 and 3, coalescence in case A2 occurs over a longer time than case A1. The longer coalescence timescale is reflected in the reconnection rate, which steadily increases with time and does not show violent fluctuations, as shown by the red curve in Fig. 5. The addition of the ionization potential in case A3 speeds up the coalescence with respect to case A2, as the current sheet thins under the action of cooling and recombination and is more compressed by the inflow. The higher mean reconnection rate of case A3, $M_{IRIP} = 0.057 \pm 0.003$, is consistent with the shorter coalescence timescale observed in Fig. 3.

In this section, we have extensively discussed the differences among NIR, IR, and IRIP coupling models for partially ionized plasmas during plasmoid coalescence. To summarize our key results, we find that ionization and recombination have a stabilizing effect on the current sheet, which is not often included in the linear theory description. Compared to fully ionized plasmas at the same bulk density, ionization and recombination still lead to a faster reconnection in PIP, and the main effects are observed in the second phase of coalescence (reconnection phase).

B. Oscillatory behaviors of the current sheet

Several types of oscillatory motions develop during plasmoid coalescence. Waves are produced in all simulations and are particularly evident in case A2 (IR model, intermediate initial coupling $\alpha_c = 100$), as shown by panels (e) and (h) of Fig. 2. Smaller scale oscillations occur in the reconnection region and along the current sheet. In this section, we describe the two main oscillatory motions that develop in the current sheet.

A first type of oscillations is linked to the increase in gas pressure in the current sheet due to the plasmoids moving closer. In our previous work, we observed a regular fluctuation in the *O*-points separation for the MHD case,[53] while such motion was suppressed in the PIP case due to the faster reconnection rate. When ionization and recombination are included (A2 and A3 cases), we find an intermediate situation between the regular peaks as in MHD and their complete absence in NIR cases, with an initial large fluctuation shown in Fig. 6 and smaller oscillations that are damped more quickly than the MHD case. The first oscillation corresponds to the large local maximum observed at the beginning of the reconnection phase for cases A2 and A3, and it is a direct consequence of the processes involved in the current sheet formation. In fact, during the current sheet formation, the plasma temperature increases in the thin region between the two initial plasmoids: the higher temperature leads to an initial burst in ionization that increases the plasma pressure at the center of the current sheet. When the plasma pressure becomes sufficiently high, it balances the pressure of the plasmoids moving closer and the plasmoids rebound off each other. At later stages, irregular oscillations of smaller magnitude can still be observed in the IR case (A2, red curve in Fig. 6), while in the IRIP case (A3, green curve), the *O*-points distance decreases steadily.

In the reconnection phase of the majority of our simulations, a second type of oscillations is observed at later times during the merging. This type of motion is displayed in Fig. 7, where the divergence of

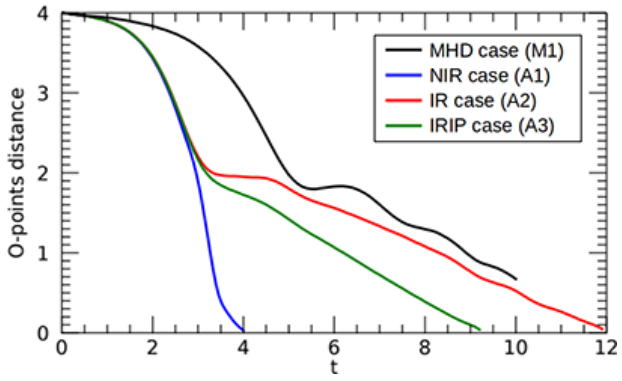

FIG. 6. Time variation of the distance between the merging plasmoids, calculated as the distance between the *O*-points for the MHD case (black) and the PIP cases A1 (blue), A2 (red), and A3 (green).

the plasma velocity is displayed in the upper half of the current sheet for a reference case (B2). Oscillations start at the jet termination shock, rapidly increasing in amplitude, and the motion propagates toward the center of the current sheet. The displacement of the current sheet center along the *x*-axis can be seen at $y = 0.3$ in all the frames of Fig. 7. For simplicity, we have displayed oscillations in a small part of the

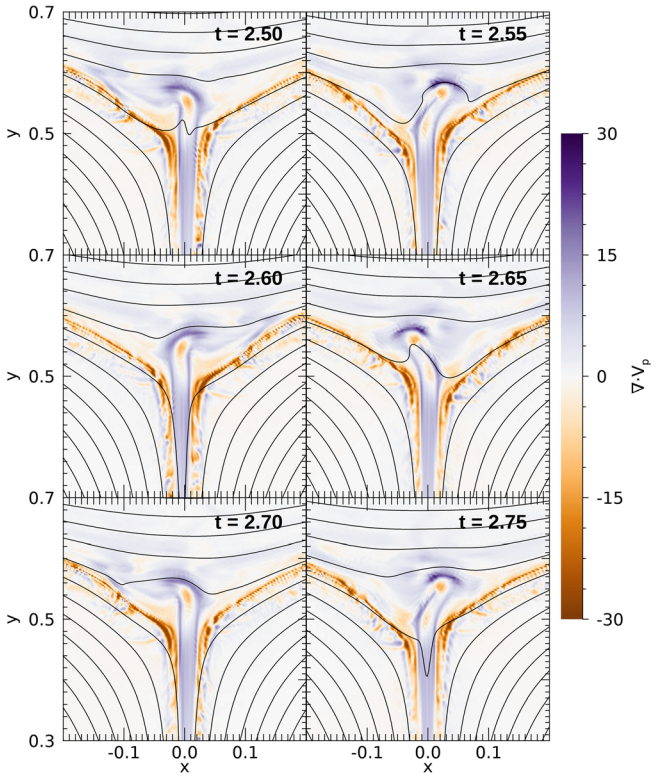

FIG. 7. Time frames of the plasma velocity divergence shown at the current sheet upper edge for the IRIP case B2. Magnetic field lines are shown in black.

domain around the current sheet. However, analogue oscillations are observed in the bottom half of the current sheet.

The oscillations are spatially resolved. We measure the displacement of the current sheet along x due to the oscillations by tracking the position in time of the peak in $|J_z|$, which corresponds to the central point of the current sheet width. In case B2, half an oscillation occurs in about $\Delta t = 0.1$, as suggested by Fig. 7. At $y = 0.3$, the distance between the peak at $t = 2.50$ (first panel in Fig. 7) and the peak at $t = 2.60$ (third panel in Fig. 7) is $\Delta l = 7.8 \times 10^{-3}$, which is four times bigger than the grid size $\Delta x = 1.95 \times 10^{-3}$. Moving toward the end of the current sheet, the oscillation amplitude increases; therefore, oscillations are resolved by a larger number of grid points.

In cases with very thin current sheets, such as A1 (NIR model) and the IRIP cases B1, B7, B8, and B9 in Table I, turbulent reconnection takes place before oscillations can develop. In fully ionized plasmas, where the current sheet is thicker, the oscillatory motion can be suppressed by increasing η. We display this change of regime by running an MHD case (M2) where we increase η by a factor of 2 ($\eta = 0.003$) from the value set for case M1 (see Table I). The current sheet of case M2 is subject to a steady, laminar reconnection, where no oscillations develop. The oscillatory behavior is, therefore, constrained by the diffusivity, whose value determines the evolution of the current sheet dynamics into either a turbulent process (lower η) or steady reconnection (higher η).

Recent high-resolution MHD simulations of fully ionized plasmas[75] have found localized nonlinear oscillations at the edges of current sheets, studied in the framework of the dynamics of flux rope eruption in solar atmospheric plasmas. In this recent study,[75] laminar reconnection occurs for a global Lundquist number $S = 2.8 \times 10^3$, and oscillations develop when the global $S = 5.5 \times 10^3$, while at high values of S ($S = 2.8 \times 10^4$), plasmoids form in the reconnecting current sheet.[75] The Lundquist numbers of our simulations are calculated by using the effective Alfvén speed $v_{A,e} \sim v_{\text{out}}$, where v_{out} is the ion outflow speed. This particular choice for approximating the Alfvén speed, consistent with our previous work,[53] accounts for the effective density given by the partial coupling between plasma and neutrals in the PIP cases. In our configuration, we observe an oscillatory behavior for Lundquist numbers between 2.6×10^3 and 3.3×10^3 in partially ionized plasma cases, while the MHD case develops this dynamics at $S = 3 \times 10^3$.

In order to better characterize the oscillatory motion, we look at the shift of the current sheet vertical axis position along x at a small distance from its center. Figure 8 shows the time variation of the plasma v_x at $x = 0$ and $y = 0.2$, closer to the center of the current sheet than the region shown in Fig. 7. As no grid point lays exactly at $x = 0$, but two sets of grid points are located at a symmetric distance from the coordinates origin, we perform a linear interpolation of the grid points located symmetrically across the y-axis. The interpolation allows to cancel out the $v_{x,p}$ contributions at the same magnitude but opposite in sign at the center of the current sheet and identify the real oscillations that displace the upper part of the structure.

The beginning of the oscillatory motion is identified in this work with the position in time of the first peak having an amplitude $v_{x,p} > 0.001$. We chose this threshold value as it is twice the magnitude of the initial white noise perturbation, so that random motions along the x-axis would not be mistaken with the beginning of the oscillations. In the case of the simulation, B2 oscillations begin at $t = 1.55$.

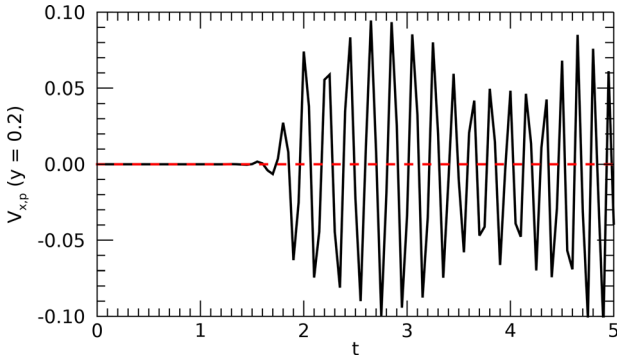

FIG. 8. Time variation of $v_{x,p}$ at $x = 0, y = 0.2$ for the IRIP case B2. This indicates the displacement of the current sheet vertical axis in the x-direction. The red dashed line indicates the value of $v_{x,p} = 0$.

We calculate the period of oscillations as the mean distance between the peaks of $v_{x,p}$ shown in Fig. 8. The oscillation periods and their error, calculated as the standard deviation of the peak separation sets of measures, are reported in Table II. Looking at the cases in the initial survey presented in Sec. III A, case A2 shows a longer period, $P_{A2} = 0.39 \pm 0.07$, than case A3, where the period is $P_{A3} = 0.22 \pm 0.04$. A period of ~0.2 has been found for all the IRIP simulations run at $\alpha_c = 5$, as shown in Table II, which is consistent with case A3 run at $\alpha_c = 100$. In the MHD case, the oscillation period is $P_{\text{MHD}} \sim 0.44$, which is comparable with the IR case A2, but approximately double than all of the IRIP cases. All the simulations are highly temporally resolved; however, the cadence of the time output is longer than the time step, with an output being saved approximately every 10^3–10^4 iterations. As our cases are analyzed post process, the chosen output might set limitations on the analysis of the period. The time outputs used in this work are $\Delta t = 0.1$ for cases M1, A2, and A3, and $\Delta t = 0.05$ for the remaining IRIP cases. These result in having about four points to determine a period in all the cases with the exception of case A3, where only two points define the period. However, the period length was confirmed through tests run by saving smaller time outputs, which prove that the oscillatory behavior has the same period.

TABLE II. Parameters of the oscillatory behavior for the 2.5D simulations. The oscillation period is presented with its standard deviation.

ID	t_{peak}	P	$\delta(t = t_{\text{peak}})$	$L(t = t_{\text{peak}})$
M1	7.1	0.44 ± 0.09	0.041	0.78
A2	5.8	0.39 ± 0.07	0.043	1.21
A3	5.7	0.22 ± 0.04	0.029	1.07
B2	1.55	0.19 ± 0.03	0.029	1.30
B3	2.10	0.20 ± 0.03	0.029	1.26
B4	1.90	0.20 ± 0.03	0.025	1.28
B5	1.75	0.15 ± 0.03	0.021	1.29
B6	1.25	0.17 ± 0.09	0.021	1.28
C1	1.15	0.20 ± 0.03	0.027	1.30
C2	2.35	0.17 ± 0.04	0.025	1.24
C3	3.35	0.14 ± 0.03	0.025	0.95

It can be suggested that the longer periods identified in both MHD and IR cases are dependent on current sheet properties. The current sheets length L and thickness δ are reported in Table II at the time t_{peak} of the first oscillation for all the cases. A correlation can be observed between oscillation period and δ: the current sheet is thicker in M1 and A2, where the period is also longer, than the IRIP cases, where the cooling from the ionization potential results in thinner current sheets.

The oscillatory dynamics does not have any influence on the reconnection rate. This can be seen through the comparison of case B2 with a second test simulation run with the same set of parameters and resolution. This second case is run in half domain in the x direction ($x = [0, 4]$), with a symmetric boundary located at $x = 0$ that prevents the onset of oscillations. Figure 9 shows the reconnection rate M of case B2 (solid black line) and the test simulation at half domain (dashed red line) where the symmetry suppresses the oscillatory motion. Both simulations display the same reconnection rate magnitude and variation across the same time interval, with minor fluctuations occurring at $t > 2$.

In this section, we have discussed the onset of oscillatory motions propagating in the current sheet. Previous works on fully ionized solar atmospheric plasmas[75,76] had observed the onset of localized oscillations in reconnecting current sheets. We find that the oscillations developing at the edges of current sheets are independent of ionization and recombination processes and more generally of partial ionization. The oscillation period shows a direct correlation with the current sheet thickness, independently of the type of plasma chosen for the simulation.

C. Secondary plasmoids

Evidence of fractal coalescence is observed in the IRIP cases B1, B7, B8, and B9, where the central current sheet is subject to the tearing instability, and secondary plasmoids are produced. Figure 10 shows the interaction of two secondary plasmoids coalescing before leaving the current sheet for case B7 in Table I.

Given the overall effects of ionization and recombination on plasmoid coalescence discussed in Sec. III A, it is interesting to examine the secondary plasmoids and compare their properties to the ones observed in NIR simulations of our previous study.[53] Ionization and recombination provide additional force terms that can be analyzed to

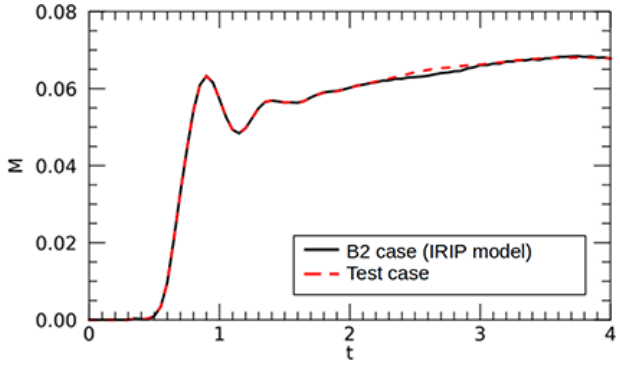

FIG. 9. Comparison of the time variation of the reconnection rate between the IRIP case B2 (solid black curve) and a test simulation run at half the domain of B2 (dashed red line). Oscillations in the test case are suppressed by the symmetric boundary set at $x = 0$.

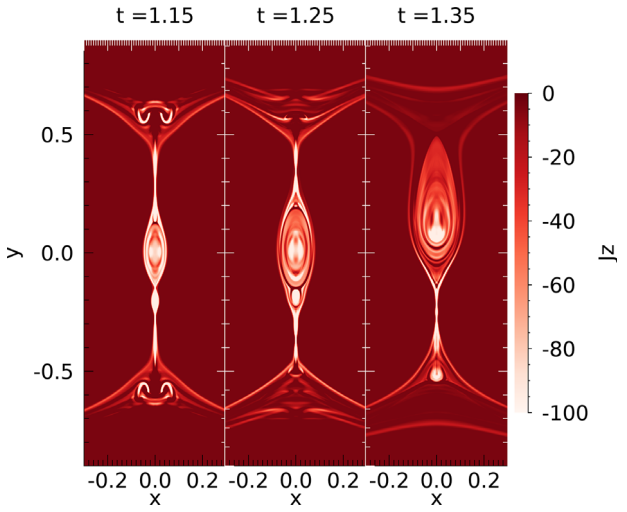

FIG. 10. Secondary plasmoid coalescence occurring in the central current sheet for the IRIP case B7. Two plasmoids are present at $t = 1.15$ (left panel). At $t = 1.25$ (central panel), the plasmoids start merging, as reconnection takes place in the current sheet located in between them. Coalescence is completed at $t = 1.35$ (right panel), and the final plasmoid moves along the current sheet to be ejected.

investigate the equilibrium of secondary plasmoids. Therefore, we look at the force balance and the magnitude of Γ_{ion} and Γ_{rec} across the two secondary plasmoids appearing on the left panel of Fig. 10 (t = 1.15) and see if the new terms shift the force balance when compared to NIR cases.[53]

The force contributions and the balance between the total pressure gradient and the Lorentz force ($\mathbf{J} \times \mathbf{B} - \nabla p$) are shown for the IRIP case B7 at $x = 0$ for $t = 1.15$ in the central panel of Fig. 11, compared to the current density magnitude map (top panel). The yellow and black vertical dashed lines in all panels are representative of the X-point location between the two plasmoids. The force components cancel each other at the plasmoids location, while the current sheet around is still out of balance. Inside the plasmoids, the major contributions to the total force are provided by the gradient of the plasma pressure (blue curve), the magnetic pressure $B^2/2$ (magenta curve), and the y-component of the magnetic tension $(\mathbf{B} \cdot \nabla) \cdot \mathbf{B}$ (red curve). This situation is similar to the cases examined in our previous study:[53] the outer structure is characterized by an almost force-free equilibrium, while $-\nabla p_p$ is significant around the plasmoid center. However, a difference is observed in the distribution of the force components in the inner structure. At the plasmoid center, we observe a magnetohydrostatic equilibrium, with both magnetic pressure and magnetic tension balancing the plasma pressure gradient, while a force-free magnetic equilibrium is sustained at the edge, where magnetic pressure and magnetic tension balance each other. Comparing the observed structure with our previous results, we see that the core region is larger in the IRIP cases than in the NIR cases. In the IRIP case, the force-free equilibrium occurs in an external thin annulus, while in NIR cases, force-free equilibrium nearly entirely dominates the plasmoid structure, with the exception of a very small region at the plasmoid center. This feature is especially evident in the larger plasmoid on the right.

Γ_{ion} (red) and Γ_{rec} (blue) are shown in the bottom panel of Fig. 11. The center of the two plasmoids, located at $y = -0.204$ for

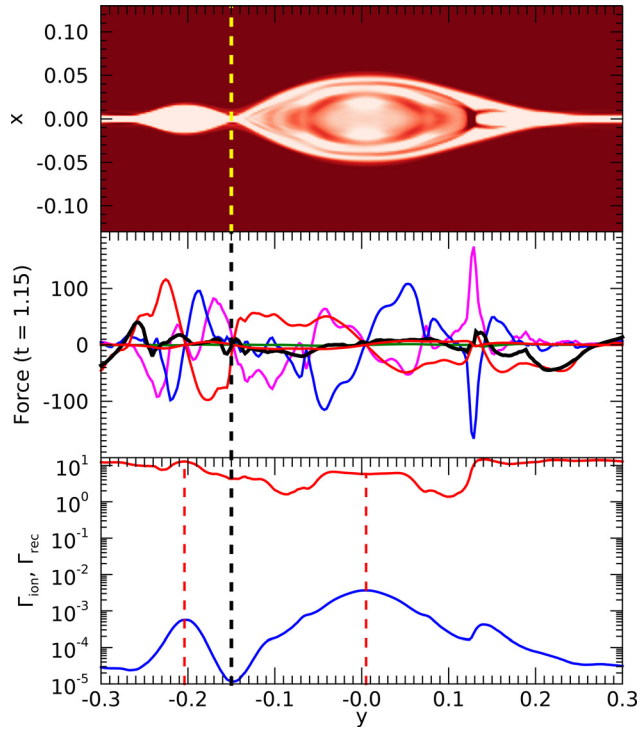

FIG. 11. Top panel: detail of the current density magnitude of secondary plasmoids at t = 1.15 in the IRIP case B7. Central panel: force balance $\mathbf{J} \times \mathbf{B} - \nabla p$ (black solid line) calculated along the current sheet in the *y*-axis, compared to the position of secondary plasmoids in the top panel. The force components are $-\nabla p_p$ (blue), $-\nabla p_n$ (green), magnetic pressure (magenta), and magnetic tension (red). Bottom panel: ionization (red) and recombination (blue) rates along the current sheet, compared to the position of secondary plasmoids in the top panel. The yellow (top panel) and black (central and bottom panels) dashed line indicate the edge between the two plasmoids. The red vertical dashed lines in the bottom panel indicate the position of the secondary plasmoids centers along the *y*-axis.

the smaller plasmoid and $y = 0.005$ for the bigger plasmoid, respectively, is indicated by the two red vertical dashed lines. Recombination is observed at very small rates along the current sheet and at the center of secondary plasmoids, while larger fluctuations are detected in the ionization rate. Both Γ_{ion} and Γ_{rec} are larger in the central part of the plasmoids, where the inner structure is in magnetohydrostatic equilibrium, while the external ring characterized by a force-free magnetic equilibrium is subject to lower change rates. While Γ_{rec} is larger at the plasmoid center and decreases toward the ends of the inner structure, the magnitude of Γ_{ion} in the bigger plasmoids tends to be slightly larger at the interface between inner and outer plasmoid regions than in the very center of the plasmoid.

Figure 12 shows the energy loss rate calculated as $A_{heat} - \Phi_I$, defined by Eqs. (27) and (28), across the secondary plasmoids at $x = 0$ and $t = 1.15$. The cooling from the term $A_{heat} - \Phi_I$ is stronger across the secondary plasmoids than the current sheet, as shown from the troughs in the energy loss rate around the location of the plasmoids centers (identified by the red dashed lines in Fig. 12). The action of the ionization potential, which corresponds to a neat temperature decrease, can contribute to the increase in the recombination rate observed inside secondary plasmoids (see bottom panel of Fig. 11).

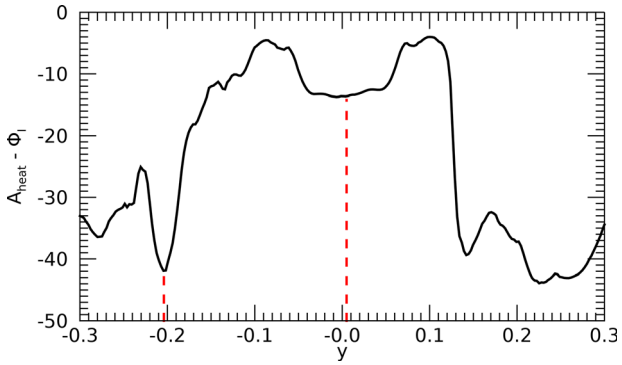

FIG. 12. Energy loss rate $A_{heat} - \Phi_I$ calculated along the current sheet ($x = 0$) at $t = 1.15$ for the IRIP case B7. The red vertical dashed lines indicate the center of the two secondary plasmoids interacting inside the current sheet.

We have seen that Γ_{ion}, Γ_{rec}, and the ionization potential modify the force distribution inside secondary plasmoids compared to NIR cases.[53] We want to evaluate whether the variation in these rates changes the force balance inside secondary plasmoids enough to modify their structure and interaction before they leave the current sheet. From the energy loss rate, we can estimate the cooling time of the plasmoid, which is calculated by dividing the total internal energy by the term $A_{heat} - \Phi_I$. At the center of the larger plasmoid, the cooling time is estimated to be $t \sim 0.7$. The expulsion time of the larger plasmoid from the current sheet is estimated to be $t \sim 0.2$, a third of the cooling time for the same plasmoid. Other smaller plasmoids coalesce or are expelled in shorter times. Therefore, we consider the secondary plasmoids to be approximately in equilibrium during their interaction inside the current sheet. Since the cooling time is larger than the expulsion time, ionization–recombination effects do not really influence the force equilibrium of the plasmoid internal structure. Despite having a slightly different internal distribution, these secondary plasmoids act in the same way as in the NIR cases discussed in our previous study.[53]

In summary, secondary plasmoids can form in the IRIP model when turbulent reconnection develops. The force balance inside these plasmoids is slightly changed under the action of ionization, recombination, and radiative losses. However, the plasmoids equilibrium and interaction inside the current sheet are unchanged when compared to previously investigated NIR cases.[53] More details on the onset of turbulent reconnection in IRIP simulations are discussed in Sec. III D.

D. Survey on τ_{IR}

The effects of the relative importance of the ionization and recombination rates and the collision rates are investigated through a survey on the parameter τ_{IR}, which is varied in the interval $[5 \times 10^{-6}, 5 \times 10^{-1}]$. The simulations listed in Table I with IDs B1–B6, characterized by a diffusivity $\eta = 1.5 \times 10^{-3}$, are compared to simulations run at a lower $\eta = 5 \times 10^{-4}$ that are listed with IDs B7–B9. Preliminary tests on 1D current sheets had shown that at lower collisional coupling, secondary plasmoids might still form, despite the stabilization of ionization and recombination on reconnection. We choose to study the coalescence for $\alpha_c = 5$, lower than the cases presented in Sec. III A, as preliminary tests have identified this collisional coupling regime to better promote the onset of nonlinear dynamics in the IRIP cases.

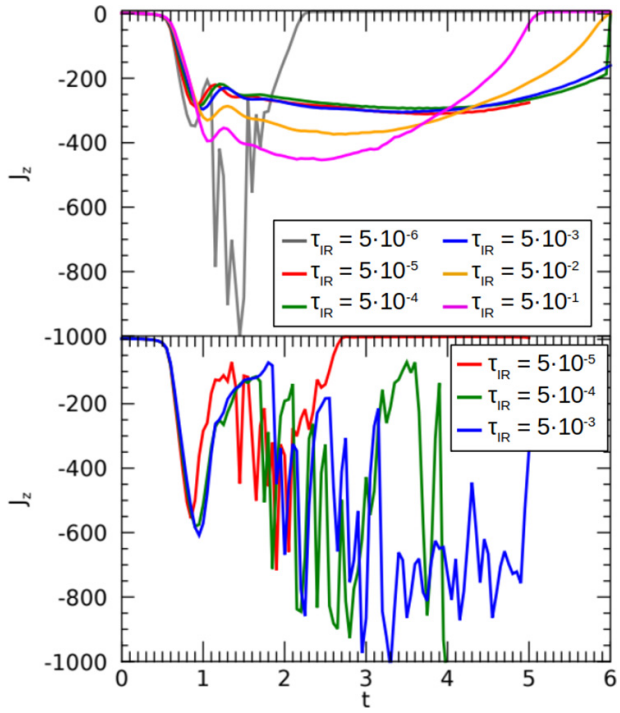

FIG. 13. Top panel: time evolution of J_z at the center of the current sheet for cases B1–B6, run at $\eta = 1.5 \times 10^{-3}$. The simulations are run at $\tau_{IR} = 5 \times 10^{-6}$ (gray), $\tau_{IR} = 5 \times 10^{-5}$ (red), $\tau_{IR} = 5 \times 10^{-4}$ (green), $\tau_{IR} = 5 \times 10^{-3}$ (blue), $\tau_{IR} = 5 \times 10^{-2}$ (orange), and $\tau_{IR} = 5 \times 10^{-1}$ (magenta). Bottom panel: time evolution of J_z at the center of the current sheet for cases B7, B8, and B9, run at $\eta = 5 \times 10^{-4}$. The simulations are run at $\tau_{IR} = 5 \times 10^{-5}$ (red), $\tau_{IR} = 5 \times 10^{-4}$ (green), and $\tau_{IR} = 5 \times 10^{-3}$ (blue).

Figure 13 shows the time variation of current density J_z at $x = 0$ and $y = 0$ for the set of simulations at higher η (top panel) and at lower η (bottom panel). The beginning of reconnection is identified with the first minimum occurring in the current density, when the current sheet is compressed the most by the two initial plasmoids. The onset of reconnection begins at similar times for all the simulations in the survey, occurring later at the increasing of τ_{IR} as ionization and recombination processes become more important in varying the plasma composition around the X-point. For both sets of simulations, the differences between these cases in the initial phase of the coalescence are small as the initial collisional coupling is very weak, and the central current sheet forms in nearly complete absence of collisions.

In the set run at $\eta = 1.5 \times 10^{-3}$ (cases B1–B6 in Table I), several differences are observed in the reconnection dynamics of each simulation. Case B1, which is run at the lowest $\tau_{IR} (= 5 \times 10^{-6})$, is the only case at higher η where secondary plasmoids formation occurs in the central current sheet, as shown by the fluctuation of the gray curve in the top panel of Fig. 13. At $\alpha_c = 5$, the fluids are weakly coupled, with 0.05 collisions due to happen in a unit of time: this aspect allows the plasma to evolve separately with respect to the neutral fluid and promotes secondary plasmoids formation. In case B1, the current sheet collapse (identified as the time between $t = 0$ and the first minimum in the current, where the current sheet is compressed the most) occurs over a period $\Delta t \sim 0.9$: at the imposed collisional coupling, we are expecting 1 collision every $\Delta t \sim 17$; therefore, we consider the current sheet formation to occur in an almost collisionless regime. The collisional ionization rate of case B1, initially 5×10^{-8}, does not significantly increase the ion fraction during the first phase of coalescence due to the lack of collisions; therefore, plasmoids can form before ionization can occur. The low ion fraction leads to a more efficient current sheet thinning, as seen in our previous paper.[53] The ejection of the first plasmoid leaves the current sheet unstable, and further smaller plasmoids are produced, leading to turbulent reconnection that efficiently reduces the coalescence timescale. Increasing τ_{IR} by one order of magnitude (case B2, red curve in the top panel of Fig. 13), the ionization rate converts a portion of neutrals large enough to increase the current sheet thickness and prevent the formation of further dynamics. For $\tau_{IR} \geq 5 \times 10^{-5}$, the tearing instability is suppressed, as the ionization rates are sufficiently high to stabilize the current sheet.

In the simulations run at $\eta = 1.5 \times 10^{-3}$, the magnitude of J_z rapidly increases with τ_{IR}, while the timescale for the plasmoid coalescence becomes considerably shorter. The faster coalescence is proven by the end time of the evolution in the top panel of Fig. 13, where the merging completion can be identified by the current density reaching positive values (at $t > 5$ for all cases with the exception of case B1, corresponding to the gray curve). The reconnection phase shortens with the thinning of the current sheet. The thinning is faster for cases where Γ_{ion} is bigger, as the cooling action of the ionization potential is proportional to the ionization rate. Increasing τ_{IR}, and consequently Γ_{ion}, reconnection becomes faster and leads to larger current densities, while the current sheet becomes thinner. In this Perspective, at $\tau_{IR} > 0.5$, we might expect a regime where the current sheet would be thin enough to promote secondary dynamics again.

In the interval of values $\tau_{IR} = [5 \times 10^{-5}, 5 \times 10^{-1}]$, the onset of the tearing instability might be achieved when a smaller diffusivity is chosen for the system, as thinner current sheets would form. For this reason, we investigate three PIP cases (B7–B9 in Table I) run with $\tau_{IR} = [5 \times 10^{-5}, 5 \times 10^{-3}]$ for a diffusivity $\eta = 5 \times 10^{-4}$. The bottom panel of Fig. 13 shows the current density at the center of the current sheet for the cases at $\tau_{IR} = 5 \times 10^{-5}$ (red), 5×10^{-4} (green), and 5×10^{-3} (blue). Secondary plasmoid formation is observed for all three cases, as the smaller resistivity leads to thinner current sheets and promotes the onset of the tearing instability. At the lowest τ_{IR}, this nonlinear dynamics shortens the coalescence timescale, as seen by the comparison of the red curves between the top and bottom panel of Fig. 13.

Figure 14 shows the Lundquist number of the simulations in the survey, calculated at the beginning of the reconnection phase by using the effective Alfvén speed $v_{A,e}$. In the cases at higher η, S decreases at the increase in τ_{IR}, increasing again for $\tau_{IR} > 0.005$. We identify a threshold for the critical Lundquist number laying in the interval $S = 5.1 \times 10^3$–7.9×10^4. The simulation at the lowest τ_{IR} (B1) is the only case at $\eta = 1.5 \times 10^{-3}$ where secondary plasmoids are seen to form in the central current sheet. The Lundquist number for this simulation is 1.07×10^4, above the critical Lundquist number. The simulations run at $\eta = 5 \times 10^{-4}$ develop plasmoid formation at Lundquist numbers ($S = 9.3 \times 10^3$ for B7, $S = 8.2 \times 10^3$ for B8, and $S = 7.9 \times 10^3$ for B9) that are consistent with the critical numbers found in our previous paper.[53]

At higher τ_{IR}, despite having a copious production of secondary plasmoids as shown by the fluctuation in the current density, the coalescence timescale is less affected by plasmoid dynamics. This effect

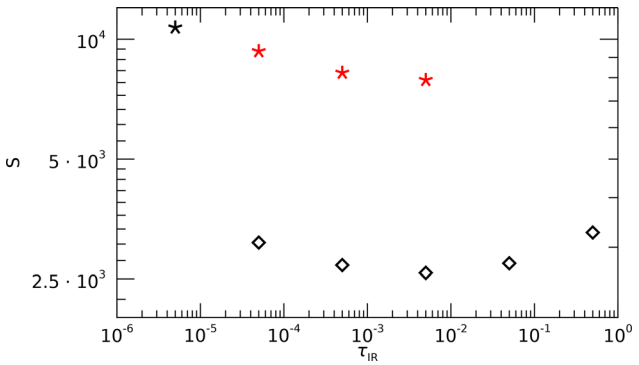

FIG. 14. Lundquist number of the τ_{IR} survey PIP simulations (B1–B9) at the beginning of the reconnection phase. Stars are associated with simulations that develop secondary plasmoids in the central current sheet, and diamonds represent simulations that do not have secondary plasmoids. Black symbols refer to the cases run at $\eta = 1.5 \times 10^{-3}$, and red symbols to the cases run at $\eta = 5 \times 10^{-4}$.

might be explained by the reconnection rate saturation already observed in many 2D MHD simulations,[30,42,75] whose study revealed that above the critical Lundquist number, the reconnection rate becomes almost independent of S, following the onset of nonlinear dynamics. Figure 15 shows a comparison between two PIP cases at $\tau_{IR} = 5 \times 10^{-3}$ that are run at two different η, for three times ($t = 1$, 3, and 5). These cases, listed as B4 and B9 in Table I, are identified by the blue curves in both top and bottom panel of Fig. 13. As shown by the direct comparison of the coalescing plasmoids size between the two cases, the coalescence proceeds at a similar timescale even though, in one case, turbulent reconnection occurs. The Lundquist numbers of the two simulations are, respectively, $S_{B4} = 2.59 \times 10^3$ and $S_{B9} = 7.89 \times 10^3$: secondary plasmoids in case B9 develop for an S consistent with the Lundquist numbers at which secondary plasmoids form in PIP of our previous paper.[53] The reconnection rate of both simulations is shown in Fig. 16. Despite having a difference in the Lundquist number, the two rates evolve in a similar way, with the larger fluctuations occurring in case B9 following the secondary plasmoid dynamics. The mean reconnection rates, calculated between $t = 1$ and $t = 5$, are, respectively, $M_{B4} = 0.062 \pm 0.004$ and $M_{B9} = 0.05 \pm 0.02$, where the errors are calculated as the standard deviation. The two rates are close, which is consistent with the effect of the reconnection rate saturation observed in other works.[30,42,75] From the Sweet–Parker steady state reconnection model, the change in η of a factor of 3 between cases B4 and B9 is expected to result in a small change of $\sim 1/\sqrt{3}$ in the reconnection rate. Re-scaling the black curve in Fig. 16 by this factor to make a prediction on the reconnection rate at lower η, we see a large difference of the predicted value with M_{B9}: the consistency between M_{B4} and M_{B9} is, therefore, not due to the small change in η leading to similar rates, but on the reconnection rate saturation itself, occurring once the turbulent reconnection is set.

The time variation of the mean plasma and neutral temperatures and the mean ionization and recombination rates inside the current

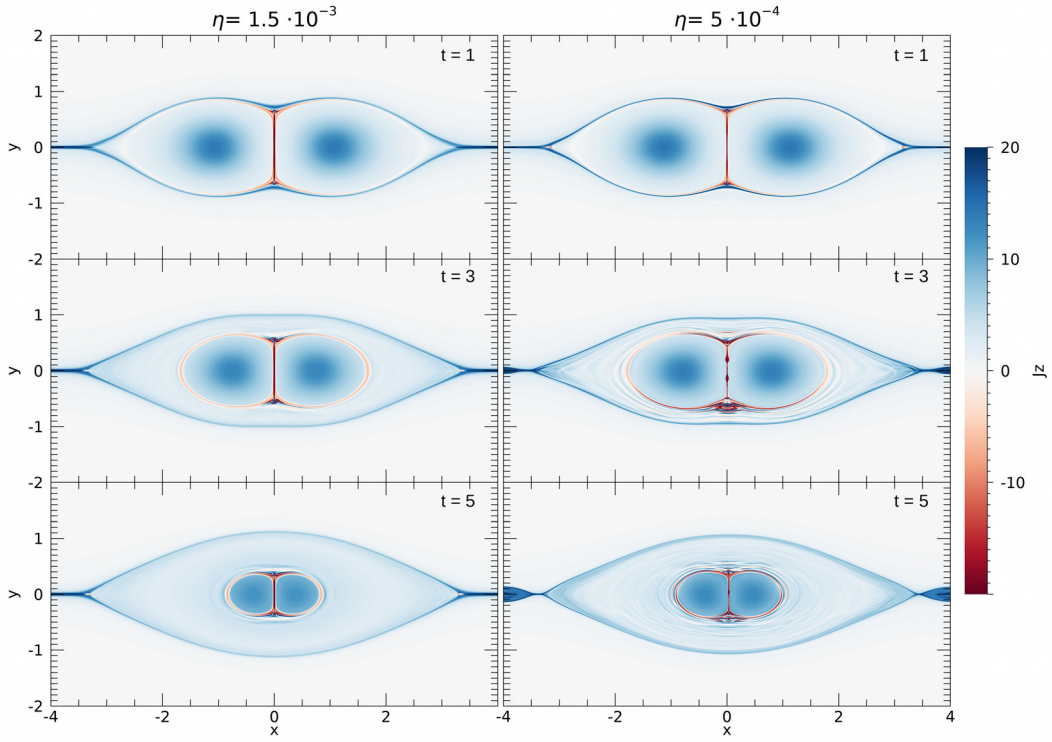

FIG. 15. Comparison of J_z between the PIP cases B4 (left column) and B9 (right column). The frames show the coalescence instability at three different times during the reconnection phase. Times are given in the same non-dimensional unit. In the case at lower η (right column), secondary plasmoids form in the central current sheet (right central and bottom panels).

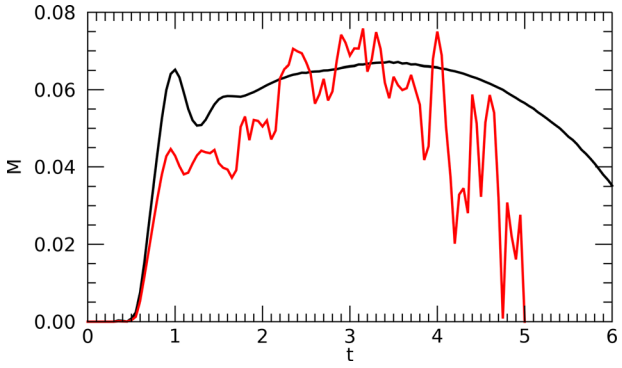

FIG. 16. Time variation of the reconnection rate for the PIP cases B4 (black curve) and B9 (red curve). The large fluctuations in case B9 depend on turbulent reconnection taking place.

sheet is shown in Fig. 17 for cases B4 (dashed lines) and B9 (solid lines). Γ_{ion} and Γ_{rec} (top panel of Fig. 17) increase in both cases in the ideal phase of coalescence following the initial ionization burst at the formation of the current sheet and are maintained approximately constant in time in the reconnection phase, with small fluctuations around the average value. The same behavior is observed in the temperature variation (bottom panel of Fig. 17). In case B4, T_p (blue dashed line) is approximately constant over the reconnection phase, while T_n (red dashed line) shows small regular fluctuations at $t > 2.5$. Plasma is colder than the neutral counterpart. This happens because reconnection leads to a high plasma temperature initially, and once ionization occurs, large amounts of plasma energy are lost and the plasma fluid cools. As the ionization burst happens over a short period of time, the timescale is not long enough for the plasma temperature to couple to

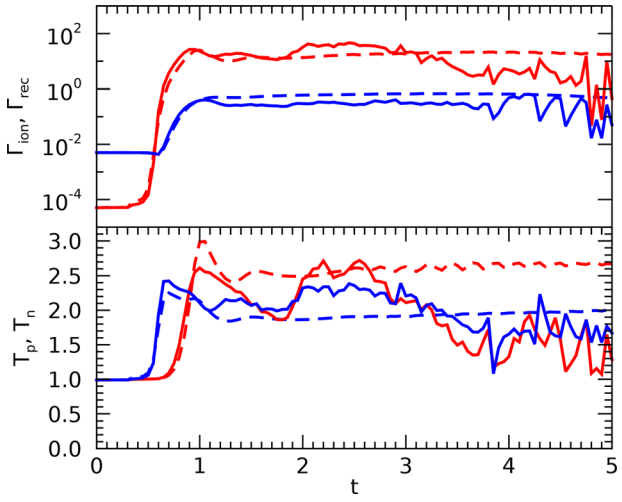

FIG. 17. Top panel: time variation of the mean ionization and recombination rates inside the current sheet for the PIP cases B4 (dashed line, $\eta = 1.5 \times 10^{-3}$) and B9 (solid line, $\eta = 5 \times 10^{-4}$). Ionization rates are shown in red, and recombination rates are shown in blue. Bottom panel: time evolution of the mean plasma (blue) and neutral (red) temperature inside the current sheet for the same PIP cases B4 (dashed line) and B9 (solid line).

the neutral temperature. In case B4, where laminar reconnection occurs, a balance is maintained with the species entering the current sheet from the inflow, and the mean temperatures vary slowly, thus leading to relatively steady ionization/recombination rates.

The fluctuations increase with the onset of the tearing instability in the current sheet as shown by the solid lines in the top panel of Fig. 17. In case B9, after an increase in temperature at the current sheet initial formation, larger fluctuations appear at the onset of tearing instability. At $t > 1$, the plasma temperature (solid blue line) is larger than case B4, while T_n is smaller. The larger T_p is the result of the larger compression of the current sheet, which is thinner in case B9. After $t \sim 3.5$, the two mean temperatures in the current sheet reach an equilibrium and fluctuate around a similar average value. The mean temperatures at $t > 3.5$ are, respectively, $T_p = 1.7 \pm 0.2$ and $T_n = 1.5 \pm 0.2$, where the ranges are calculated as the standard deviation of the measures. At later stages, there is also a general decrease in both Γ_{ion} and Γ_{rec} in case B9, while in case B4, the rates remain constant. The large fluctuations in the presence of secondary plasmoids dynamics depend on the different mechanisms of expulsion of the plasma from the unstable current sheet. The neutral temperature decreases at later times in correspondence of secondary plasmoids formation – and consequently does Γ_{ion} – and equals the plasma temperature, whose magnitude is comparable to the case without tearing instability (B4).

In this section, we investigate the relative importance of Γ_{ion} and Γ_{rec} to the collisional coupling α_c on determining the type of reconnection during plasmoid coalescence. Because of the nature of the coalescence instability and the large compression of the current sheet in a small time interval, very small ionization/recombination rates ($\tau_{IR} \sim 5 \times 10^{-5}$) are capable to affect the reconnection dynamics, as they are very sensible to temperature changes. Turbulent reconnection in weakly coupled plasmas is promoted either for nearly negligible ionization/recombination rates ($\tau_{IR} \sim 5 \times 10^{-6}$) or by reducing η, which directly affects the Lundquist number.

E. Survey on the ion fraction

We investigate the changes in the coalescence dynamics of the IRIP cases following a variation of the initial ion fraction ξ_p. The parameter ξ_p depends directly on the reference temperature T_0, selected at the beginning of calculation. Therefore, we evaluate changes in the coalescence instability by progressively increase T_0 by 1000 K. We compare four calculations, listed as C1, B2, C2, and C3 in Table I, where we vary the reference temperature in the range $T_0 = [9855, 12\,855]$ K.

Figure 18 shows the time variation of J_z at the center of the current sheet for the four IRIP cases. The changes in T_0 correspond to an ion fraction variation in the range $\xi_p = [2 \times 10^{-3}, 10^{-1}]$. Note that in all cases, we consider a medium that is initially dominated by neutrals.

The coalescence timescale is drastically reduced at the decrease in temperature and consequently ion fraction. The timescale shortening, involving both ideal phase (initial attraction of the plasmoids to each other) and reconnection phase, is explained by the variation of the effective Alfvén speed, which scales as $1/\sqrt{\xi_p}$. The increased Alfvén speed allows more flux to enter the reconnection region, hence feeding the reconnection process and accelerating it.

In terms of the observed trend in the development of the current density magnitude, this survey reproduces the results of our previous paper's study on ξ_p.[53] Going toward higher ξ_p, where the magnetic

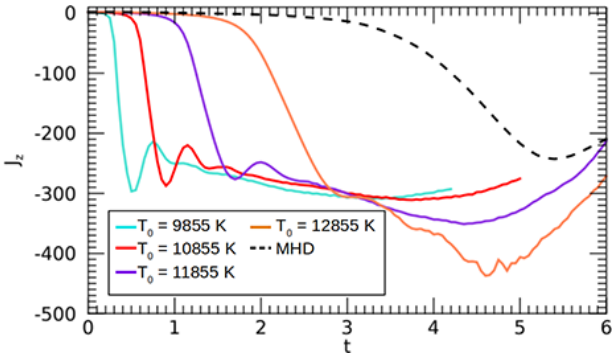

FIG. 18. Time evolution of current density J_z at the center of the current sheet for four PIP cases (C1, C2, C3, and B2). The initial reference temperature T_0 is $T_0 = 9855$ K, corresponding to an initial $\xi_p = 2 \times 10^{-3}$ (turquoise), 10855 K, corresponding to $\xi_p = 10^{-2}$ (red), 11 855 K, corresponding to $\xi_p = 4 \times 10^{-2}$ (purple), and 12 855 K, corresponding to $\xi_p = 10^{-1}$ (orange). The current density of an MHD case (M1) is included as comparison to the limit $T_0 \to \infty$.

forces are felt by larger portions of the uid, the coalescence timescale tends to the MHD case. The reconnection rate increases slightly as $\xi_p(0)$ increases. This trend, shown by the values of the mean reconnection rate collected in Table III, is opposite of what was observed in our previous paper.[53] The reversal in trend might be explained by examining both the variation in plasma and neutral densities across the current sheet, and the average ionization and recombination rates. Figure 19 shows the mean values of Γ_{ion} and Γ_{rec} (top panel) and of ρ_p and ρ_n (bottom panel) across the current sheet for the four cases presented in the survey. The oscillations of the average value of ρ_p and ρ_n can be associated with the oscillatory motion of the current sheet.

The compression of the current sheet by the merging plasmoids results in heating that leads to a burst in ionization, observed in particular, at the formation of the current sheet. At the increase in the initial ξ_p, both Γ_{ion} and Γ_{rec} decrease inside the current sheet, as shown in the top panel of Fig. 19. This is due to the larger ρ_p at the center of the structure, as the plasma pressure prevents the current sheet to thin more, hence showing a smaller temperature change. When the ionization rate is small, it leads to a limited ionization, which also turns into a lesser thinning of the current sheet as the cooling action of the ionization potential is reduced. The lower cooling affects the recombination rate, whose decrease leads to fewer neutrals forming and leaving the current sheet.

Having an initial lower ξ_p and, consequently, a larger ionization rate due to the initial current sheet thinning, both ρ_p and ρ_n increase more inside the current sheet, the latter due to the larger cooling factor provided by the ionization potential. Although the coalescence is faster for lower $\xi_p(t = 0)$, the local increase in density leads to a comparable reconnection rate for all the cases in this survey.

TABLE III. Initial ion fraction $\xi_p(0)$, the mean reconnection rate M, and the Lundquist number S of cases C1, B2, C2, and C3, run for the survey on the ion fraction. Errors on the reconnection rate are calculated as the standard deviation.

ID	$\xi_p(0)$	M	S
C1	2×10^{-3}	0.063 ± 0.005	2.7×10^3
B2	10^{-2}	0.063 ± 0.005	3.1×10^3
C2	4×10^{-2}	0.067 ± 0.008	5.1×10^3
C3	10^{-1}	0.08 ± 0.01	4.9×10^3

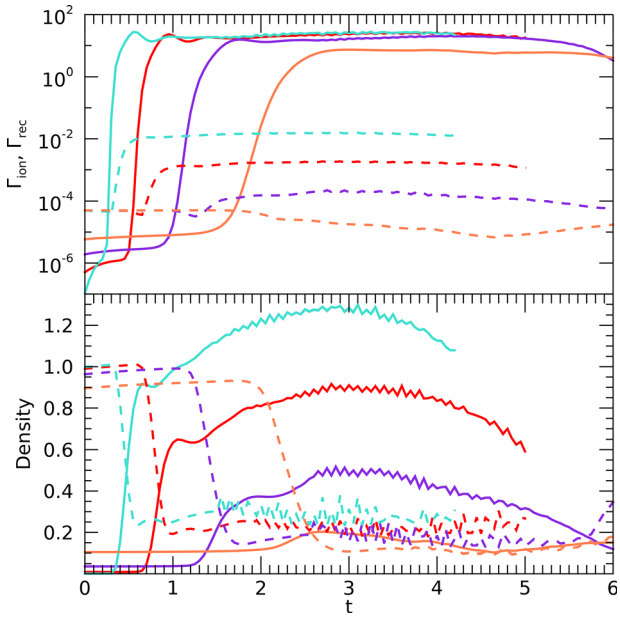

FIG. 19. Top panel: time variation of the mean ionization (solid lines) and recombination rates (dashed lines) averaged over the current sheet for cases C1 (turquoise), B2 (red), C2 (purple), and C3 (orange). Bottom panel: time variation of the mean values of ρ_p (solid lines) and ρ_n (dashed lines) inside the current sheet for cases C1 (turquoise), B2 (red), C2 (purple), and C3 (orange). The oscillations observed in the density are related to the oscillatory motion of the current sheet.

The change of the effective Alfvén speed and plasma density affects the Lundquist number, which, in turn, extends the timescale of the reconnection phase. The values for the Lundquist number calculated at the beginning of the reconnection phase are shown in Table III, and it is shown that the Lundquist number also slightly increases in the interval. The value of S for case C3 ($\xi_p = 10^{-1}$) is consistent with our previous study without ionization and recombination.[53] At lower $\xi_p(t = 0)$, the Lundquist number is generally lower than our previous work, but this is due to the increase in plasma density that comes from the ionization at the center of the current sheet.

In general, the evolution of the coalescence instability observed from changes in the current density follows the same trend as the NIR cases previously studied.[53] However, ionization/recombination rates act on both the reconnection rate M and the Lundquist number S. Both parameters vary less than the NIR simulations in the same $\xi_p(0)$ interval.

IV. DISCUSSION

Plasmoid coalescence is a very important process for promoting fast magnetic reconnection in many reconnecting systems: in fact, plasmoids allow the shortening of the timescale for explosive events by acting on the size of reconnecting current sheets. It is not entirely clear about how coalescence develops in a partially ionized plasma, and in particular, how it is affected by the charge-neutral species interaction.

In this work, we have extended our previous study on the coalescence instability in partially ionized plasmas[53] by including ionization, recombination, and optically thin radiative losses in the two-fluid coupling terms. The goal of our update is to model a more realistic coupling between different particle species during coalescence. We have observed several changes in the development of this instability that are related to the newly included two-fluid physics:

(1) Ionization and recombination have a stabilizing effect on the current sheet as they are responsible for thickening it, but still lead to a faster reconnection in PIP when compared to MHD cases at the same bulk density.
(2) The formation of the central current sheet begins at similar times for all PIP cases at the same initial collisional coupling, with or without ionization and recombination, ionization potential, and background heating. This is because in the first phase of coalescence, the rates are in equilibrium, and the temperature on which they depend does not show sharp variation. During the reconnection phases, where the temperature increases, ionization/recombination effects dominate the reconnection dynamics and are responsible for the type of reconnection that develops in the current sheet.
(3) The internal structure of secondary plasmoids is slightly altered under the action of ionization and recombination: a larger part of their structure is in magnetohydrostatic equilibrium, while the external region characterized by a force-free equilibrium is reduced to a thin annulus. However, the secondary plasmoid dynamics inside the current sheet is unchanged when compared to NIR cases.[53]
(4) Small initial ionization/recombination rates (∼five orders of magnitude smaller than the collision rates) in weakly ionized plasmas can still lead to an efficient stabilization of the current sheet against the tearing instability in the reconnection phase. This happens because the temperature increases locally, enhancing the rates by several orders of magnitude inside the current sheet, thus leading to a substantial increase in ρ_p inside the current sheet.
(5) When varying the initial ion fraction, the general development of the coalescence is unchanged from NIR cases, but ionization and recombination influence the reconnection rate and the Lundquist number because they increase locally the plasma density, thus affecting the value of the effective Alfvén speed.

In addition to the results that are directly dependent on the presence of ionization/recombination rates, we also find that in cases of laminar reconnection, the current sheet develops an oscillatory behavior in the outflow that is independent of partial ionization effects and correlated with the current sheet thickness (see Fig. 7).

From our findings, the stabilization factor in (1) provides interesting consequences for a recent paper[44] that had investigated fractal reconnection in partially ionized plasmas in strongly, intermediate, and weakly coupled regimes. As changes in the ionization level directly affect the current sheet evolution, then the time scales for fractal tearing previously identified[44] will be largely affected by the presence of ionization–recombination processes. The local dynamics observed in (1) and (2) is also consistent with the ionization bursts found in previous studies on magnetic reconnection in multi-fluid partially ionized plasmas.[7,42,43,46–48]

We conclude with the implications of our findings for chromospheric reconnection. The chromospheric rates of ionization and recombination are typically[49,74] in the range 10^{-5}–10^{-3} s^{-1}, between two and seven orders of magnitude smaller than the typical chromospheric neutral-ion collision frequency (10^{-1}–10^{2} s^{-1}).[77–79] Our study, where rates are set consistent with the chromospheric values, demonstrates that ionization and recombination rates are large enough to suppress the onset of fractal coalescence and small-scale dynamics, as they act on current sheets properties. However, multi-fluid physics is still capable to promote fast reconnection, hence explaining the short time scales of chromospheric explosive events. A process that is not accounted for in this work is the interaction of the plasma with the photospheric radiation field. While collisional ionization by electrons is important for heavier elements, photo-ionization is the predominant process for ionizing hydrogen in the chromosphere[64] and leads to a hydrogen ionization rate[65,66] $\Gamma_{ion}^{ph} \sim 1.4 \times 10^{-2}$ s^{-1} that can become orders of magnitude bigger than collisional ionization by electrons[66,80] $\Gamma_{ion} \sim 7.8 \times 10^{-5}$ s^{-1}. The inclusion of photo-ionization would impose changes in the balance between ions and neutrals as a function of the atmospheric temperature; therefore, it will be a subject for further updates of our model.

ACKNOWLEDGMENTS

The authors are grateful to Dr. N. Nakamura for the inspiration of his original work on this problem that leads to this study. A.H. and B.S. are supported by STFC Research Grants Nos. ST/R000891/1 and ST/V000659/1.

This work used the DiRAC@Durham facility managed by the Institute for Computational Cosmology on behalf of the STFC DiRAC HPC Facility (www.dirac.ac.uk). The equipment was funded by BEIS capital funding via STFC capital Grant Nos. ST/P002293/1, ST/R002371/1, and ST/S002502/1, Durham University, and STFC operations Grant No. ST/R000832/1. DiRAC is part of the National e-Infrastructure.

AUTHOR DECLARATIONS

Conflict of Interest

The authors have no conflicts to disclose.

DATA AVAILABILITY

The data that support the findings of this study are openly available in (PIP) at https://github.com/GiuliaMurtas/PIP.git and https://github.com/AstroSnow/PIP, Refs. 53 and 54.

REFERENCES

[1]E. G. Zweibel and M. Yamada, "Magnetic reconnection in astrophysical and laboratory plasmas," Annu. Rev. Astron. Astrophys. **47**, 291–332 (2009).
[2]D. Biskamp, *Magnetic Reconnection in Plasmas*, Cambridge Monographs on Plasma Physics Vol. 3 (Cambridge University Press, Cambridge, UK, 2000), p. 387.
[3]E. Priest and T. Forbes, *Magnetic Reconnection: MHD Theory and Applications/Eric Priest* (2000).
[4]K. Shibata, T. Nakamura, T. Matsumoto, K. Otsuji, T. J. Okamoto, N. Nishizuka, T. Kawate, H. Watanabe, S. Nagata, S. Ueno, R. Kitai, S. Nozawa, S. Tsuneta, Y. Suematsu, K. Ichimoto, T. Shimizu, Y. Katsukawa, T. D. Tarbell, T. E. Berger, B. W. Lites, R. A. Shine, and A. M. Title, "Chromospheric anemone jets as evidence of ubiquitous reconnection," Science **318**, 1591 (2007).

[5]N. Nishizuka, T. Nakamura, T. Kawate, K. A. P. Singh, and K. Shibata, "Statistical study of chromospheric anemone jets observed with Hinode/SOT," Astrophys. J. **731**, 43 (2011).
[6]F. Ellerman, "Solar hydrogen 'bombs,'" Astrophys. J. **46**, 298 (1917).
[7]L. Ni, V. S. Lukin, N. A. Murphy, and J. Lin, "Magnetic reconnection in the low solar chromosphere with a more realistic radiative cooling model," Phys. Plasmas **25**, 042903 (2018).
[8]K. A. P. Singh, K. Shibata, N. Nishizuka, and H. Isobe, "Chromospheric anemone jets and magnetic reconnection in partially ionized solar atmosphere," Phys. Plasmas **18**, 111210 (2011).
[9]K. A. P. Singh, H. Isobe, N. Nishizuka, K. Nishida, and K. Shibata, "Multiple plasma ejections and intermittent nature of magnetic reconnection in solar chromospheric anemone jets," Astrophys. J. **759**, 33 (2012).
[10]L.-J. Guo, B. D. Pontieu, Y.-M. Huang, H. Peter, and A. Bhattacharjee, "Observations and modeling of the onset of fast reconnection in the solar transition region," Astrophys. J. **901**, 148 (2020).
[11]H. P. Furth, J. Killeen, and M. N. Rosenbluth, "Finite-resistivity instabilities of a sheet pinch," Phys. Fluids **6**, 459–484 (1963).
[12]S. Tanuma, T. Yokoyama, T. Kudoh, and K. Shibata, "Two-dimensional magnetohydrodynamic numerical simulations of magnetic reconnection triggered by a supernova shock in the interstellar medium: Generation of x-ray gas in the galaxy," Astrophys. J. **551**, 312–332 (2001).
[13]K. Shibata and S. Tanuma, "Plasmoid-induced-reconnection and fractal reconnection," Earth, Planets, Space **53**, 473–482 (2001).
[14]R. Samtaney, N. F. Loureiro, D. A. Uzdensky, A. A. Schekochihin, and S. C. Cowley, "Formation of plasmoid chains in magnetic reconnection," Phys. Rev. Lett. **103**, 105004 (2009).
[15]N. F. Loureiro, A. A. Schekochihin, and S. C. Cowley, "Instability of current sheets and formation of plasmoid chains," Phys. Plasmas **14**, 100703 (2007).
[16]N. F. Loureiro, R. Samtaney, A. A. Schekochihin, and D. A. Uzdensky, "Magnetic reconnection and stochastic plasmoid chains in high-Lundquist-number plasmas," Phys. Plasmas **19**, 042303 (2012).
[17]N. F. Loureiro and D. A. Uzdensky, "Magnetic reconnection: From the Sweet-Parker model to stochastic plasmoid chains," Plasma Phys. Controlled Fusion **58**, 014021 (2016).
[18]E. G. Zweibel, "Magnetic reconnection in partially ionized gases," Astrophys. J. **340**, 550 (1989).
[19]S. Takeshige, S. Takasao, and K. Shibata, "A theoretical model of a thinning current sheet in the low-β plasmas," Astrophys. J. **807**, 159 (2015).
[20]L. Ni, B. Kliem, J. Lin, and N. Wu, "Fast magnetic reconnection in the solar chromosphere mediated by the plasmoid instability," Astrophys. J. **799**, 79 (2015).
[21]W. Park, D. A. Monticello, and R. B. White, "Reconnection rates of magnetic fields including the effects of viscosity," Phys. Fluids **27**, 137–149 (1984).
[22]R. S. Steinolfson and G. van Hoven, "Nonlinear evolution of the resistive tearing mode," Phys. Fluids **27**, 1207–1214 (1984).
[23]D. Biskamp, "Magnetic reconnection via current sheets," Phys. Fluids **29**, 1520–1531 (1986).
[24]L. C. Lee and Z. F. Fu, "Multiple X line reconnection 1. A criterion for the transition from a single X line to a multiple X line reconnection," J. Geophys. Res. **91**, 6807–6815, https://doi.org/10.1029/JA091iA06p06807 (1986).
[25]S. P. Jin and W. H. Ip, "Two-dimensional compressible magnetohydrodynamic simulation of the driven reconnection process," Phys. Fluids B **3**, 1927–1936 (1991).
[26]M. Ugai, "Computer studies on powerful magnetic energy conversion by the spontaneous fast reconnection mechanism," Phys. Plasmas **2**, 388–397 (1995).
[27]N. F. Loureiro, S. C. Cowley, W. D. Dorland, M. G. Haines, and A. A. Schekochihin, "X-point collapse and saturation in the nonlinear tearing mode reconnection," Phys. Rev. Lett. **95**, 235003 (2005).
[28]T. Tajima, J. Sakai, H. Nakajima, T. Kosugi, F. Brunel, and M. R. Kundu, "Current loop coalescence model of solar flares," Astrophys. J. **321**, 1031 (1987).
[29]M. Bárta, J. Büchner, M. Karlický, and P. Kotrč, "Spontaneous current-layer fragmentation and cascading reconnection in solar flares. II. Relation to observations," Astrophys. J. **730**, 47 (2011).
[30]A. Bhattacharjee, Y.-M. Huang, H. Yang, and B. Rogers, "Fast reconnection in high-Lundquist-number plasmas due to the plasmoid instability," Phys. Plasmas **16**, 112102 (2009).
[31]P. A. Cassak, M. A. Shay, and J. F. Drake, "Scaling of Sweet-Parker reconnection with secondary islands," Phys. Plasmas **16**, 120702 (2009).
[32]Y.-M. Huang and A. Bhattacharjee, "Scaling laws of resistive magnetohydrodynamic reconnection in the high-Lundquist-number, plasmoid-unstable regime," Phys. Plasmas **17**, 062104 (2010).
[33]L. Ni, K. Germaschewski, Y.-M. Huang, B. P. Sullivan, H. Yang, and A. Bhattacharjee, "Linear plasmoid instability of thin current sheets with shear flow," Phys. Plasmas **17**, 052109 (2010).
[34]L. Ni, U. Ziegler, Y.-M. Huang, J. Lin, and Z. Mei, "Effects of plasma β on the plasmoid instability," Phys. Plasmas **19**, 072902 (2012).
[35]L. Ni, J. Lin, and N. A. Murphy, "Effects of the non-uniform initial environment and the guide field on the plasmoid instability," Phys. Plasmas **20**, 061206 (2013).
[36]T. Tajima and J. I. Sakai, "Explosive coalescence of magnetic islands," IEEE Trans. Plasma Sci. **14**, 929–933 (1986).
[37]J. E. Vernazza, E. H. Avrett, and R. Loeser, "Structure of the solar chromosphere. III. Models of the EUV brightness components of the quiet sun," Astrophys. J., Suppl. Ser. **45**, 635–725 (1981).
[38]G. W. Pneuman, S. K. Solanki, and J. O. Stenflo, "Structure and merging of solar magnetic fluxtubes," Astron. Astrophys. **154**, 231–242 (1986).
[39]E. H. Avrett and R. Loeser, "Models of the solar chromosphere and transition region from SUMER and HRTS observations: formation of the extreme-ultraviolet spectrum of hydrogen, carbon, and oxygen," Astrophys. J., Suppl. Ser. **175**, 229–276 (2008).
[40]E. Khomenko, M. Collados, and T. Felipe, "Nonlinear numerical simulations of magneto-acoustic wave propagation in small-scale flux tubes," Sol. Phys. **251**, 589–611 (2008).
[41]E. G. Zweibel, E. Lawrence, J. Yoo, H. Ji, M. Yamada, and L. M. Malyshkin, "Magnetic reconnection in partially ionized plasmas," Phys. Plasmas **18**, 111211 (2011).
[42]J. E. Leake, V. S. Lukin, M. G. Linton, and E. T. Meier, "Multi-fluid simulations of chromospheric magnetic reconnection in a weakly ionized reacting plasma," Astrophys. J. **760**, 109 (2012).
[43]J. E. Leake, V. S. Lukin, and M. G. Linton, "Magnetic reconnection in a weakly ionized plasma," Phys. Plasmas **20**, 061202 (2013).
[44]K. A. P. Singh, A. Hillier, H. Isobe, and K. Shibata, "Nonlinear instability and intermittent nature of magnetic reconnection in solar chromosphere," Publ. Astron. Soc. Jpn. **67**, 96 (2015).
[45]G. S. Voronov, "A practical fit formula for ionization rate coefficients of atoms and ions by electron impact: Z = 1–28," At. Data Nucl. Data Tables **65**, 1–35 (1997).
[46]L. Ni and V. S. Lukin, "Onset of secondary instabilities and plasma heating during magnetic reconnection in strongly magnetized regions of the low solar atmosphere," Astrophys. J. **868**, 144 (2018).
[47]N. A. Murphy and V. S. Lukin, "Asymmetric magnetic reconnection in weakly ionized chromospheric plasmas," Astrophys. J. **805**, 134 (2015).
[48]L. Ni, V. S. Lukin, N. A. Murphy, and J. Lin, "Magnetic reconnection in strongly magnetized regions of the low solar chromosphere," Astrophys. J. **852**, 95 (2018).
[49]B. Snow and A. Hillier, "Collisional ionisation, recombination, and ionisation potential in two-fluid slow-mode shocks: Analytical and numerical results," Astron. Astrophys. **645**, A81 (2021).
[50]V. L. Dorman and R. M. Kulsrud, "One-dimensional merging of magnetic fields with cooling," Astrophys. J. **449**, 777 (1995).
[51]D. A. Uzdensky and J. C. McKinney, "Magnetic reconnection with radiative cooling. I. Optically thin regime," Phys. Plasmas **18**, 042105–042105 (2011).
[52]A. Alvarez Laguna, A. Lani, N. N. Mansour, H. Deconinck, and S. Poedts, "Effect of radiation on chromospheric magnetic reconnection: Reactive and collisional multi-fluid simulations," Astrophys. J. **842**, 117 (2017).
[53]G. Murtas, A. Hillier, and B. Snow, "Coalescence instability in chromospheric partially ionized plasmas," Phys. Plasmas **28**, 032901 (2021).
[54]A. Hillier, S. Takasao, and N. Nakamura, "The formation and evolution of reconnection-driven, slow-mode shocks in a partially ionised plasma," Astron. Astrophys. **591**, A112 (2016).
[55]A. Hillier, "Ion-neutral decoupling in the nonlinear Kelvin-Helmholtz instability: Case of field-aligned flow," Phys. Plasmas **26**, 082902 (2019).

[56]S. I. Braginskii, "Transport processes in a plasma," Rev. Plasma Phys. **1**, 205 (1965).
[57]E. T. Meier and U. Shumlak, "A general nonlinear fluid model for reacting plasma-neutral mixtures," Phys. Plasmas **19**, 072508 (2012).
[58]A. Vögler, S. Shelyag, M. Schüssler, F. Cattaneo, T. Emonet, and T. Linde, "Simulations of magneto-convection in the solar photosphere. Equations, methods, and results of the MURaM code," Astron. Astrophys. **429**, 335–351 (2005).
[59]B. T. Draine, "Multicomponent, reacting MHD flows," Mon. Not. R. Astron. Soc. **220**, 133–148 (1986).
[60]G. P. Zank, L. Adhikari, L. L. Zhao, P. Mostafavi, E. J. Zirnstein, and D. J. McComas, "The pickup ion-mediated solar wind," Astrophys. J. **869**, 23 (2018).
[61]B. M. Smirnov, *Physics of Atoms and Ions* (Springer, 2003).
[62]K. L. Bell, H. B. Gilbody, J. G. Hughes, A. E. Kingston, and F. J. Smith, "Recommended data on the electron impact ionization of light atoms and ions," J. Phys. Chem. Ref. Data **12**, 891–916 (1983).
[63]M. A. Lennon, K. L. Bell, H. B. Gilbody, J. G. Hughes, A. E. Kingston, M. J. Murray, and F. J. Smith, "Recommended data on the electron impact ionization of atoms and ions: fluorine to nickel," J. Phys. Chem. Ref. Data **17**, 1285–1363 (1988).
[64]J. Geiss and P. Bochsler, "Ion composition in the solar wind in relation to solar abundances," in *CNES Isotopic Ratios in the Solar System* (Paris: Editions CNES, 1985), pp. 213–228.
[65]R. von Steiger and J. Geiss, "Supply of fractionated gases to the corona," Astron. Astrophys. **225**, 222–238 (1989).
[66]H. Peter and E. Marsch, "Hydrogen and helium in the solar chromosphere: A background model for fractionation," Astron. Astrophys. **333**, 1069–1081 (1998).
[67]V. M. Fadeev, I. F. Kvabtskhava, and N. N. Komarov, "Self-focusing of local plasma currents," Nucl. Fusion **5**, 202–209 (1965).
[68]T. D. Arber, G. J. J. Botha, and C. S. Brady, "Effect of solar chromospheric neutrals on equilibrium field structures," Astrophys. J. **705**, 1183–1188 (2009).
[69]E. G. Harris, "On a plasma sheath separating regions of oppositely directed magnetic field," Il Nuovo Cimento **23**, 115–121 (1962).
[70]J. M. Finn and P. K. Kaw, "Coalescence instability of magnetic islands," Phys. Fluids **20**, 72–78 (1977).
[71]J. C. Dorelli and J. Birn, "Electron magnetohydrodynamic simulations of magnetic island coalescence," Phys. Plasmas **8**, 4010–4019 (2001).
[72]D. A. Knoll and L. Chacón, "Coalescence of magnetic islands in the low-resistivity, hall-MHD regime," Phys. Rev. Lett. **96**, 135001 (2006).
[73]K. D. Makwana, R. Keppens, and G. Lapenta, "Study of magnetic reconnection in large-scale magnetic island coalescence via spatially coupled MHD and PIC simulations," Phys. Plasmas **25**, 082904 (2018).
[74]M. Carlsson and R. F. Stein, "Dynamic hydrogen ionization," Astrophys. J. **572**, 626–635 (2002).
[75]T. Takahashi, J. Qiu, and K. Shibata, "Quasi-periodic oscillations in flares and coronal mass ejections associated with magnetic reconnection," Astrophys. J. **848**, 102 (2017).
[76]S. Takasao and K. Shibata, "Above-the-loop-top oscillation and quasi-periodic coronal wave generation in solar flares," Astrophys. J. **823**, 150 (2016).
[77]J. E. Leake, T. D. Arber, and M. L. Khodachenko, "Collisional dissipation of Alfvén waves in a partially ionised solar chromosphere," Astron. Astrophys. **442**, 1091–1098 (2005).
[78]E. Khomenko and M. Collados Vera, "Simulations of chromospheric heating by ambipolar diffusion," in *Second ATST-EAST Meeting: Magnetic Fields from the Photosphere to the Corona*, edited by T. R. Rimmele, A. Tritschler, F. Wöger, M. Collados Vera, H. Socas-Navarro, R. Schlichenmaier, M. Carlsson, T. Berger, A. Cadavid, P. R. Gilbert, P. R. Goode, and M. Knölker (Astronomical Society of the Pacific, 2012), Vol. 463, p. 281.
[79]B. Popescu Braileanu, V. S. Lukin, E. Khomenko, and Á. de Vicente, "Two-fluid simulations of waves in the solar chromosphere. I. Numerical code verification," Astron. Astrophys. **627**, A25 (2019).
[80]W. Lotz, "Electron-impact ionization cross-sections and ionization rate coefficients for atoms and ions," Astrophys. J., Suppl. Ser. **14**, 207 (1967).